

Distributed multi-parameter quantum metrology with a superconducting quantum network

Jiajian Zhang,^{1,2,3,*} Lingna Wang,^{4,*} Yong-Ju Hai,^{1,2,*} Jiawei Zhang,^{1,2,3,*} Ji Chu,² Ji Jiang,^{1,2,3} Wenhui Huang,^{1,2,3} Yongqi Liang,^{1,2,3} Jiawei Qiu,^{1,2,3} Xuandong Sun,^{1,2,3} Ziyu Tao,² Libo Zhang,^{1,2,3} Yuxuan Zhou,² Yuanzhen Chen,^{1,2,3,5} Weijie Guo,² Xiayu Linpeng,² Song Liu,^{1,2,3,6} Wenhui Ren,² Jingjing Niu,^{2,6,†} Youpeng Zhong,^{1,2,3,6,‡} Haidong Yuan,^{4,§} and Dapeng Yu^{1,2,3,5,6}

¹*Shenzhen Institute for Quantum Science and Engineering,
Southern University of Science and Technology, Shenzhen 518055, China*

²*International Quantum Academy, Shenzhen 518048, China*

³*Guangdong Provincial Key Laboratory of Quantum Science and Engineering,
Southern University of Science and Technology, Shenzhen 518055, China*

⁴*Department of Mechanical and Automation Engineering,
The Chinese University of Hong Kong, Shatin, Hong Kong*

⁵*Department of Physics, Southern University of Science and Technology, Shenzhen 518055, China*

⁶*Shenzhen Branch, Hefei National Laboratory, Shenzhen 518048, China*

Quantum metrology has emerged as a powerful tool for timekeeping, field sensing, and precision measurements within fundamental physics. With the advent of distributed quantum metrology, its capabilities have been extended to probing spatially distributed parameters across networked quantum systems. However, generating the necessary non-local entanglement remains a significant challenge, and the inherent incompatibility in multi-parameter quantum estimation affects ultimate performance. Here we use a superconducting quantum network with low-loss interconnects to estimate multiple distributed parameters associated with non-commuting generators. By employing high-fidelity non-local entanglement across network nodes and a sequential control strategy, we accurately estimate remote vector fields and their gradients. Our approach achieves an improvement of up to 6.86 dB over classical strategy for estimating all three components of a remote vector field in terms of standard deviation. Moreover, for the estimation of gradients along two distinct directions across distributed vector fields, our distributed strategy, which utilizes non-local entanglement, outperforms local entanglement strategies, leading to a 3.44 dB reduction in the sum of variances.

The quest for high-precision measurement is fundamental to scientific advancement. Quantum metrology, which exploits quantum mechanical phenomena such as superposition and entanglement, seeks to improve measurement precision beyond classical limits¹⁻⁷. Distributed Quantum Metrology (DQM), which utilizes net-

works of spatially distributed quantum sensors to investigate the characteristics of remote signals or the collective properties of signals spread across various locations^{2,8-16}, has gained increased attention due to its broad applications. These include multidimensional parameter estimation in geology and astronomy^{17,18}, as well as the global synchronization of clocks¹⁹⁻²². The development of large-scale entangled networks is particularly promising, presenting new opportunities for enhanced precision in metrological tasks^{1,23-27}. Recent progress in photonic^{3,28-31} and atomic sensor networks^{32,33}, has shown that entanglement across distributed nodes can significantly improve the precision of estimating a single property of distributed signals, such as the average of multiple distributed phases associated with commuting generators. However, the practical implementation of DQM confronts significant hurdles. Firstly, maintaining high-fidelity quantum states over appreciable distances as well as scaling entanglement across complex networks remains difficult. Secondly, scaling metrological protocols to accommodate multi-parameter estimation requires innovative theoretical frameworks. Overcoming these obstacles in experimental hardware and metrological strategies is crucial for unlocking the full potential of DQM and advancing measurement precision across multiple disciplines.

Recent experimental advancements with superconducting qubits have highlighted their adaptability and promise in quantum sensing^{4,34-36}, showcasing potential implications in dark matter detection³⁷⁻⁴⁰. Moreover, the rapid evolution of superconducting quantum networks⁴¹⁻⁴⁸, propelled by the demand for large-scale expansion, has achieved high-quality interconnects and multi-qubit entanglement generation between modules⁴⁹, positioning these networks as an ideal platform for implementing distributed quantum sensing.

In this study, we implement distributed multi-parameter quantum metrology on a modular superconducting quantum architecture. Modular quantum architectures provide a scalable solution by linking multiple

* These authors contributed equally to this work.

† niujj@iqasz.cn

‡ zhongyp@sustech.edu.cn

§ hdyuan@mae.cuhk.edu.hk

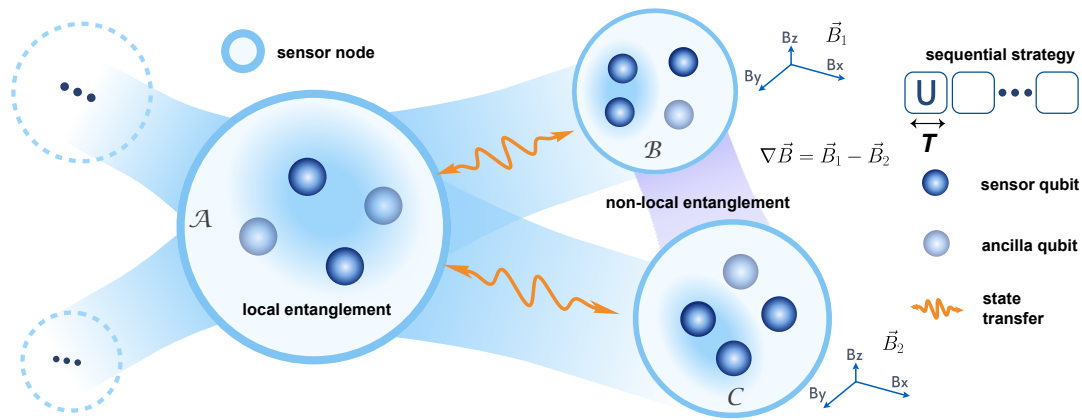


Fig. 1. **Schematic of distributed quantum metrology with a sensor network.** The advantage of quantum metrology in this hardware is enhanced by incorporating both the scaling of intra- and inter-modular entanglement and exerting the time resource with so-called sequential strategy. Along with appropriate probe state, measurement and parameter estimation, this network becomes a flexible platform for detecting non-local vector field signals.

specialized quantum processors into a unified network. These modules, each optimized for specific tasks such as memory storage^{25,31,50}, data processing⁵¹, error correction^{52,53}, and sensing^{54,55}, are connected via quantum links^{25,31,50,52}. Utilizing high-fidelity, deterministic intra-node state transfer, we build non-local entanglement between the central modular and a sensor modular to estimate all three components of a remote three-dimensional vector field, achieve a precision gain of up to 6.86 dB below the classical limit in terms of standard deviation. Subsequently, we expand our protocol by creating a 4-qubit distributed Greenberger-Horne-Zeilinger (GHZ) state across two sensor modules via inter-node state transfer through the central module. This enables the direct estimation of gradients along two distinct directions across distributed vector fields, resulting in a metrological gain of 3.44 dB over local strategies.

Experimental setup

The experimental setup, as depicted in Fig. 1, presents a quantum network composed of multiple sensor nodes linked to a central node⁴⁹, establishing a platform for non-local entanglement generation and quantum state transfer between nodes. The network consists of multiple modules, each with four qubits, arranged in a star topology. Four 25-centimeter aluminum coaxial cables provide low-loss connections between the peripheral modules and the central module (A), with each cable-qubit interface equipped with a tunable coupler. These cables act as resonator buses, hosting a series of standing wave modes that mediate microwave photon transfer from one qubit to another across modules. Through carefully coordinated control of qubit and coupler operations, this setup achieves an optimal balance between the fidelity of state transfer and qubit coherence, with inter-module transfer efficiencies approaching 99%. Non-local entanglement is realized by transferring a qubit from a locally prepared Bell state to a distant module, enabling scal-

able and versatile quantum sensing strategies across distributed nodes.

Utilizing non-local entanglement, we conduct two experiments. In the first experiment, we first create a maximally entangled state between the central module and one sensor module. This is done by initially generating an entangled state locally on the central module, then transferring a single-qubit part of the state to a sensor qubit on the sensor module, and the rest qubit on the central module serves as an ancilla. We then use this entangled state to simultaneously estimate three components of a vector field situated at the sensor module. In the second experiment, we involve two sensor modules and establish entanglement between them. This process begins with the local generation of an entangled state on the central module, followed by the transfer of distinct parts of the state to each sensor module through inter-modular quantum state transfer. This entangled state is then employed to estimate the multiple gradients of two vector fields located at the sensor modules. For both sensing protocols, we apply maximum likelihood estimation (MLE) for data analysis to determine the unknown physical parameters from the measurement results (see Methods for details). These estimations enable us to evaluate the precision and robustness of the parameter estimation.

Sensing of remote vector fields

We first demonstrate the simultaneous estimation of three components of a remote vector field located at one sensor node. In this scenario, we simulate a setup where the central module can perform measurements and entangled operations, whereas the sensor module, which interacts with the vector field, is restricted to local operations. This configuration is common in numerous applications.

The experiment procedure is illustrated in Fig. 2a. Initially, we generate a Bell state $|\psi\rangle = \frac{1}{\sqrt{2}}(|00\rangle + |11\rangle)$ in the central module A. We retain one qubit, denoted as Q_1 ,

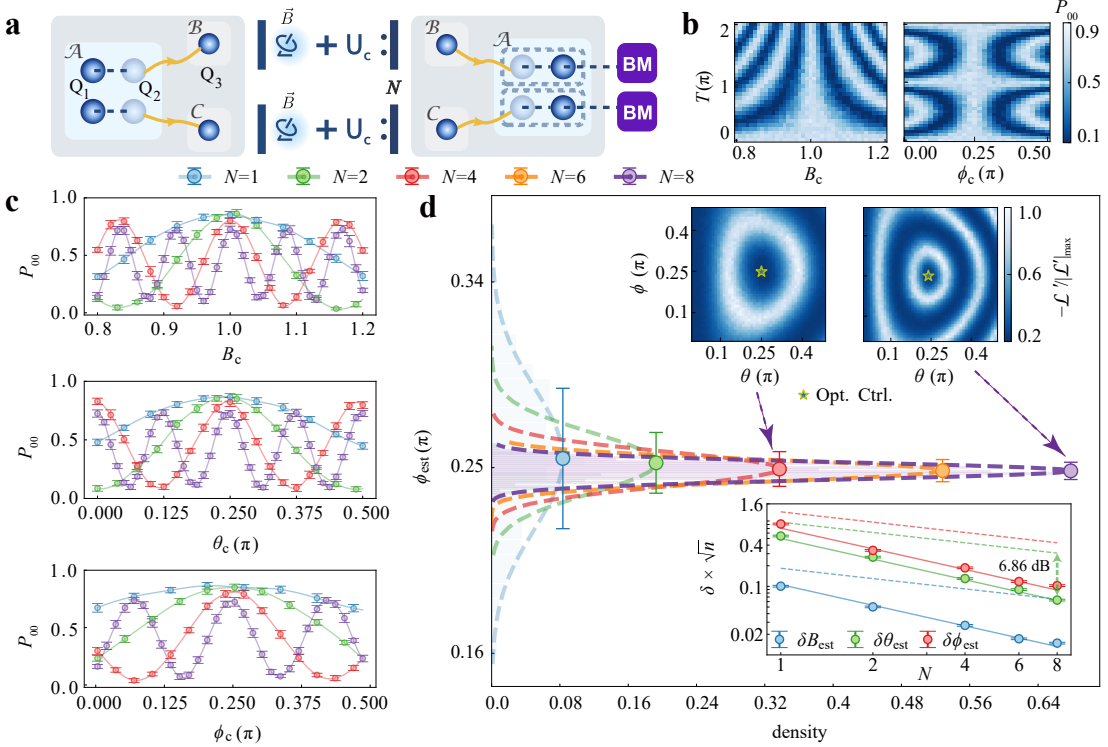


Fig. 2. Separate metrology of local magnetic field with the sensor-ancilla network. **a**, Schematic diagram of the separate-measurement strategy. The metrology of a local magnetic field distributed at positions where the sensors are deployed. We use the sequential strategy with one ancilla qubit to measure \vec{B}_1, \vec{B}_2 , which are both three-component magnetic field with parameters: $\{B, \theta, \phi\}$. **b**, Probability P_{00} measured at $N = 8$ with signal encoding times T from 0 to 2π , across varying control parameters B_c (left panel) and ϕ_c (right panel). **c**, Probability P_{00} measured at various cycle number $N = 1, 2, 4, 8$ and a fixed encoding time $T = 1.5\pi$, with varying control parameters $\{B_c, \theta_c, \phi_c\}$. The control parameters not varied in **b** and **c** are fixed to their optimal values. **d**, Results of parameter estimation. Main panel: Distribution of estimator ϕ_{est} for $N = 1, 2, 4, 6, 8$ (dashed lines represent Gaussian fitting of the estimator histogram; circles and the error bars mark the average value of ϕ_{est} and the standard deviation). Upper inset: Landscape of the likelihood function at $N = 4$ (left) and $N = 8$ (right) for parameters ϕ and θ . Lower inset: Assessed precision of the three parameters (dots) compared to their Heisenberg limits (solid lines) and the classical bound (dashed lines), extracted from $M = 600$ sets of estimators, each estimator is derived from $n = 600$ repeats of single-shot measurement. The dashed arrow: the gain of $\delta\theta_{\text{est}}$ over its classical bound.

on module \mathcal{A} and transfer the state of the other qubit, denoted as Q_2 , to qubit Q_3 on a sensor module \mathcal{B} , where the vector field is located. This establishes a Bell state between Q_1 and Q_3 that spans module \mathcal{A} and \mathcal{B} (see Supplementary Information, Section II.C). Q_3 then interacts with the vector field with the signal unitary represented by $U_s(\hat{x}) = e^{-i\vec{B}\cdot\sigma T}$, where $\hat{x} = (B, \theta, \phi)$, to encode the parameters to the probe state. For simplicity, we use spherical coordinates (B, θ, ϕ) instead of Cartesian coordinates, $\vec{B} = (B \sin \theta \cos \phi, B \sin \theta \sin \phi, B \cos \theta)$, σ is the vector of Pauli matrices and T is the signal encoding time. Subsequently, a control unitary U_c is applied to the sensor qubit. The sequence of signal and control unitaries is repeated N times so the total evolution is given by $[U_c U_s(\hat{x})]^N \otimes I$. We can optimize the control operation to improve the precision. Theoretically, the optimal control is given by $U_c = U_s^\dagger(\hat{x})$ ^{56–60}. In practice, as the parameters are initially unknown, the control needs to be im-

plemented adaptively, $U_c = U_s^\dagger(\hat{x}_c)$ where $\hat{x}_c = (B_c, \theta_c, \phi_c)$ are the estimated values of $\hat{x} = (B, \theta, \phi)$ obtained from the prior knowledge and adaptively updated with the accumulation of measurement data. Finally, the state of Q_3 is transferred back to Q_2 in module \mathcal{A} where a projective measurement on the Bell states is performed. By repeating the experiment n times, we obtain the probability of the measurement results, $\{P_{00}, P_{01}, P_{10}, P_{11}\}$, from which the estimators of the parameters can be obtained via MLE. By performing the procedure a total of M times, we can obtain M estimators, which allows us to calculate the standard deviation of the estimation. This process can be similarly applied to estimate fields at other sensor modules, and it can be parallelized as shown in Fig. 2a.

In our experiment, we configured the parameters to $B = 1$ and set θ and ϕ to $\frac{\pi}{4}$. With optimal control in place, the total evolution simplifies to $U = I \otimes I$, im-

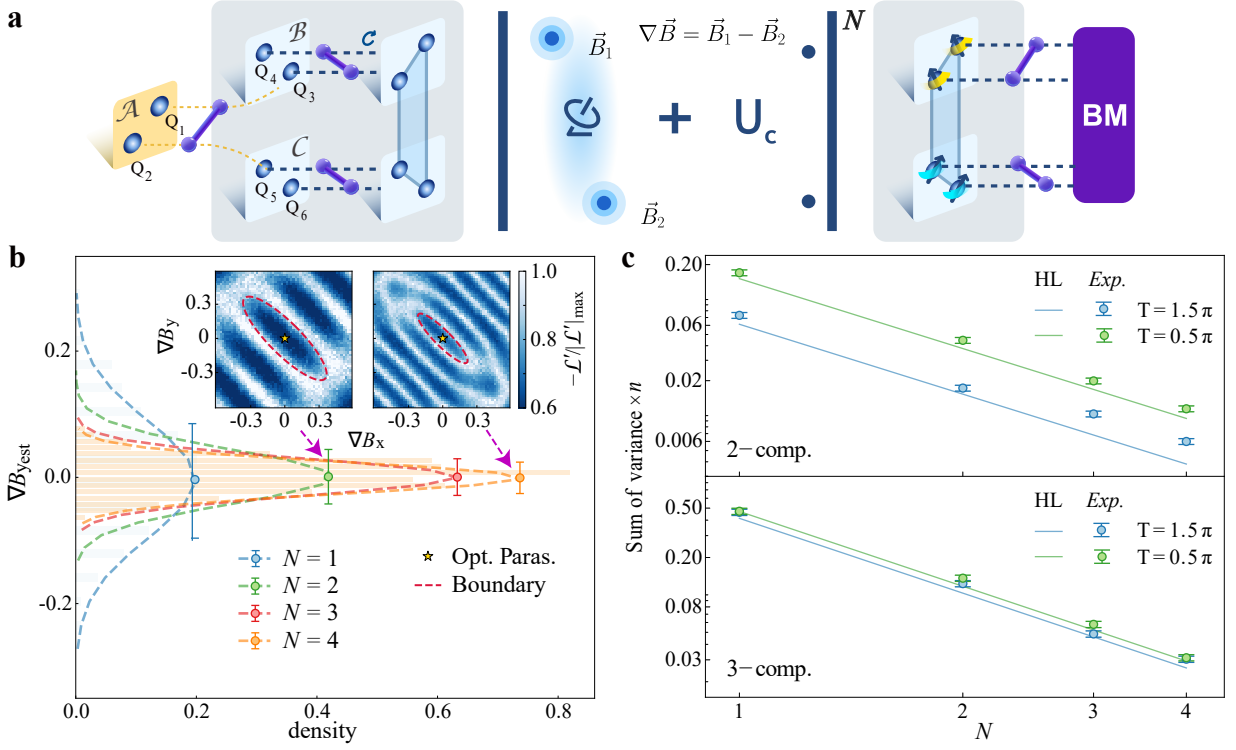


Fig. 3. Directly metrology of the magnetic field gradient. **a**, Distributed sensing scheme for directly estimating the gradients of two vector fields using NLE. Left section shows the probe state initialization. The system consists of a central module (yellow box) and two sensor modules (light blue boxes within the grey area). Blue spheres within the modules represent qubits, the purple stick-ball model represents CNOT gates, and the circular arrow denotes a local rotation. Four sensor qubits are initialized in a non-local probe state, $|\Psi_0\rangle = \frac{1}{\sqrt{2}}(|0011\rangle - |1100\rangle)$. The middle section illustrates the signal control encoding process, while the right section depicts simultaneous Bell measurements on the two encoded sensor modules. Sensor qubits in the same colored stripes are encoded with identical signals. **b**, Benchmarking the performance of the gradiometer. Main panel: Distribution of estimator $\{\nabla B_{y_{\text{est}}}\}$ for $N = 1$ to $N = 4$. Dashed lines represent the Gaussian fit of the estimator histograms, while circles and error bars indicate the mean values and standard deviations ($\delta \nabla B_{y_{\text{est}}}$). Inset: Landscape of the likelihood function \mathcal{L}' at $N = 2$ (left) and $N = 4$ (right). **c**, The gradient estimation precision, evaluated by the sum of variances, $\sum_{i \in \{x, y, z\} \cup \{x, y\}} \delta^2 \nabla B_{i_{\text{est}}}$, obtained from M sets of estimators ($M = 600$), each derived from n measurement shots ($n = 600$). Top panel: 2-component vector field. Bottom panel: 3-component vector field. Solid lines indicate the Heisenberg limit (HL). Precision estimated at $T = 0.5\pi$ is marked in green, while precision at $T = 1.5\pi$ is marked in blue.

plying that the final state matches the initially prepared Bell state. Consequently, the experimental measurement probability peaks at P_{00} . In Fig. 2b, we plot the profile of P_{00} with respect to the control parameter B_c and ϕ_c across different values of T where the width of the central peak serves as an indicator of the estimation precision for the corresponding parameters. Notably, for a given N , the precision for each parameter does not indefinitely improve with increased T . The peak width for B narrows, while for ϕ it oscillates as T increases. We then set $T = 1.5\pi$ and scan the control parameters individually. The resulting probabilities, as depicted in Fig. 2c, demonstrate a consistent reduction in the width of the central peak, signifying improved estimation precision for all three parameters as N increases.

To assess measurement precision, we apply the maximum likelihood to yield a set of estimates $\hat{x}_{\text{est}} = (B_{\text{est}}, \theta_{\text{est}}, \phi_{\text{est}})$. As an example, Fig. 2d displays the esti-

mator for ϕ , ϕ_{est} . The Gaussian distribution reveals the boundary within the parameter estimation space, with saddle points signifying the alignment of signal parameters with optimal control parameters. Importantly, as the number of cycles N increases, the boundary contracts, reflecting the enhanced precision of the sequential protocol. Additionally, by varying signal parameters θ and ϕ and obtaining P_i , $i \in \{00, 01, 10, 11\}$, we construct the 2D likelihood landscape of $P_i(\hat{x}, \hat{x}_c)$, illustrating how the reduced area with increasing N corresponds to a decreased standard deviation in parameter estimates. As shown in the lower inset of Fig. 2d, the precision for all three estimators, $B_{\text{est}}, \theta_{\text{est}}, \phi_{\text{est}}$ reaches the Heisenberg limit, and the precision for each parameter aligns with the highest precision attainable in single-parameter scenarios, indicating zero trade-offs (see Methods). In terms of standard deviation, the maximal precision gains we achieve for $B_{\text{est}}, \theta_{\text{est}}, \phi_{\text{est}}$ are 6.40 dB, 6.86 dB, 6.28 dB, respec-

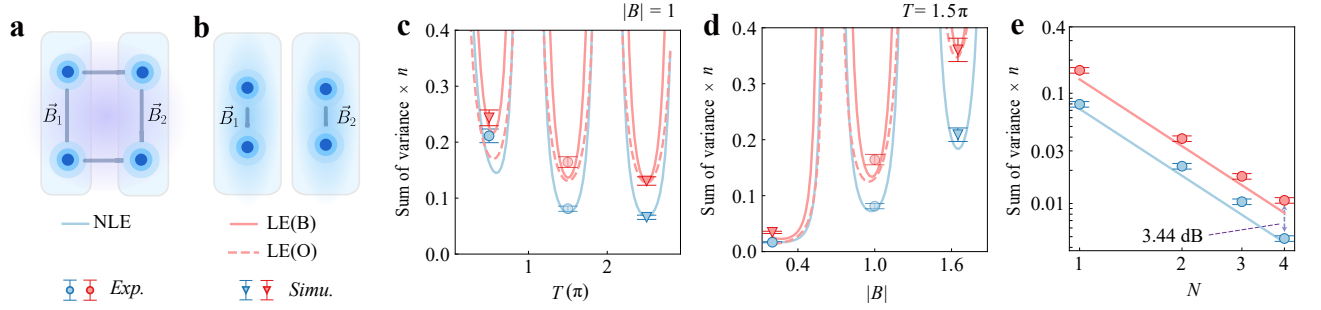


Fig. 4. **Strategies comparison for gradient estimation of a 2-component vector field.** **a-b**, Schematic diagrams of different strategies: **(a)** Distributed sensing with non-local entanglement (NLE); **(b)** Sensing with local entanglement (LE). **c-e**, Comparison of the precision ($\sum_{i \in \{x,y\}} \delta^2 \nabla B_{i\text{est}}$) of the two strategies. **(c)** Precision versus $|B|$ for the three strategies at $T = 1.5\pi$ and $N = 1$. **(d)** Impact of T on estimation precision at $|B| = 1$ and $N = 1$. **(e)** Estimation precision versus N for the three strategies at $T = 1.5\pi$ and $|B| = 1$. The solid and dashed curves: the theoretical precision bound. LE(B): local entanglement strategy using Bell state as the probe state, and Bell measurement. LE(O): local entanglement strategy using the optimal probe state and measurement.

tively.

Distributed sensing of vector field gradients

In the second experiment, we do not put any restrictions on the capability of the sensor modules. Local entangled operations and measurements can be performed on the sensor modules. Our objective is to implement the gradiometer across two sensor modules where two vector fields, \vec{B}_1 and \vec{B}_2 are located separately, and simultaneously estimate all components of the gradients $\nabla \vec{B} = \vec{B}_1 - \vec{B}_2$.

We first prepare a non-local entangled state $|\Psi_0\rangle = (|0011\rangle - |1100\rangle)/\sqrt{2}$ across sensor modules (\mathcal{B} and \mathcal{C}). This starts with generating a Bell pair between qubits Q_1 and Q_2 in the central module \mathcal{A} , followed by synchronizing its distribution from Q_1 to Q_3 on module \mathcal{B} , and Q_2 to Q_5 on \mathcal{C} using a hybrid quantum state transfer scheme. Immediately thereafter, we apply CNOT gates on both \mathcal{B} and \mathcal{C} , and obtain the GHZ state across module \mathcal{B} and \mathcal{C} . The probe state $|\Psi_0\rangle$ is obtained by applying additional X gates on Q_3 and Q_4 , and a Z gate on Q_5 . In our experiment, the preparation has a fidelity of 76.16% in total.

The entangled state then interacts with local vector fields \vec{B}_1 and \vec{B}_2 , with the free evolution over T units of time described by the operator $U_S(\vec{B}_1, \vec{B}_2) = U_{s1}^{\otimes 2} \otimes U_{s2}^{\otimes 2}$, where $U_{sj} = e^{-i\vec{B}_j \cdot \sigma T}$ for $j = 1, 2$. This evolution operator can be reparametrized as $U_S(\nabla \vec{B}, \sum \vec{B})$, with $\nabla \vec{B} = \vec{B}_1 - \vec{B}_2$ representing the gradient and $\sum \vec{B} = \vec{B}_1 + \vec{B}_2$. In our experiment, a control operation U_C is applied following each free evolution, and this cycle is repeated N times, resulting in a total evolution of $[U_C U_S(\nabla \vec{B}, \sum \vec{B})]^N$. The information is then extracted through Bell measurements conducted in both modules \mathcal{B} and \mathcal{C} . Similar to previous schemes, the control is implemented adaptively, $U_C = U_S^\dagger(\nabla \vec{B}_C, \sum \vec{B}_C)$ where $(\nabla \vec{B}_C, \sum \vec{B}_C)$ are the iteratively refined estimates of $(\nabla \vec{B}, \sum \vec{B})$ based on accumulated measurement data. The experiment is conducted n times, resulting in a set

of probability distributions, $\{P_{ijkl}\}$ where $i, j, k, l \in \{0, 1\}$. Utilizing these probabilities, we estimate the gradient $\nabla \vec{B}_{\text{est}} = (\nabla B_x, \nabla B_y, \nabla B_z)$ using the maximum-likelihood function (refer to the Methods section for more details).

To validate this protocol, we consider two instances of \vec{B}_1 and \vec{B}_2 . The first is $\vec{B}_1 = \vec{B}_2 = \sqrt{2}/4(1, 1, 0)$, representing two vector fields in the XY-plane with the Z-component known to be 0. The second is $\vec{B}_1 = \vec{B}_2 = (\frac{1}{2}, \frac{1}{2}, \frac{\sqrt{2}}{2})$, two three-dimensional vector fields. Here, without loss of generality, we take $\vec{B}_1 = \vec{B}_2$ since when $\vec{B}_1 \neq \vec{B}_2$, we can adaptively add $\nabla \vec{B}_{\text{est}}$ at site 2, which asymptotically makes them equal and does not affect the asymptotic performance. In both scenarios, we conduct the experiment for N values ranging from 1 to 4. As illustrated in Fig. 3c, the precision obtained from the experiment approaches the theoretical limit and achieves the Heisenberg scaling.

Under Bell measurement, the probabilities of the measurement results are dominated by P_{0010} and P_{1000} (see Supplementary Information, Section II.C). Using the y -component estimator ($\nabla B_{y\text{est}}$) as an example, its normalized distribution (Fig. 3b) shows that as N ranging from 1 to 4 at $T = 1.5\pi$, the standard deviation $\delta \nabla B_{y\text{est}}$ (represented by error bars), gradually decreases, signifying enhanced estimation precision. Likewise, the performance for the x -component, $\delta \nabla B_{x\text{est}}$, follows the same trend (see Supplementary Information, Section II.C and III.B).

For comparison, we conduct another experiment with only local entanglement (LE) within the modules (see Fig. 4b). In this approach, maximally entangled states are generated within each module to estimate \vec{B}_1 and \vec{B}_2 separately. The evolution is similarly interspersed with optimal controls and Bell measurements are performed on the final states. The gradient is then computed from these two local estimations, with both qubits in each module functioning as sensors.

We compare the LE strategy to the NLE strategy by using the ratio of the sum of variances from

each approach. This is expressed as $g_{\text{LE/NLE}} = 10 \log_{10}[(\sum_{i \in \{x,y\}} \delta^2 \nabla B_{i_{\text{est}}})_{\text{LE}}^{\text{exp(sim)}} / (\sum_{i \in \{x,y\}} \delta^2 \nabla B_{i_{\text{est}}})_{\text{NLE}}^{\text{exp}}]$. We evaluate this ratio at various parameter values to assess the performance of the strategies. We first choose $|B| = 1$ and change the encoding time T ranging from 0.5π to 2.5π , as illustrated in Fig. 4c. Next, we fix $T = 1.5\pi$, and demonstrate the precision for $|B|$ ranging from 0.2 to 1.65 (see Fig. 4d). Finally, we focus on $|B| = 1$ and $T = 1.5\pi$, and validate that both strategies can be enhanced by sequential copies of the encoding process, the maximal gain of the NLE strategy over LE strategy is achieved up to $g_{\text{LE/NLE}} = 3.44$ dB for $N = 4$.

Summary

Through the deterministic generation of high-fidelity non-local entanglement across network nodes, our experiment demonstrates Heisenberg scaling for the estimation of all three components of a remote vector field, with an improvement of up to 6.86 dB over classical strate-

gies in terms of standard deviation. In the context of gradient estimation, our distributed strategy, which capitalizes on deterministically generated non-local entanglement, surpasses local strategies, achieving a 3.44 dB reduction in the sum of variances when estimating gradients across two distinct directions within distributed two-dimensional vector fields.

These advancements in distributed multi-parameter quantum metrology have broad implications across various scientific and technological domains. For instance, in geology and astronomy, our method could facilitate more precise estimation of multidimensional parameters, enhancing our understanding of celestial bodies and geological structures. We anticipate that our findings will inspire more practical applications of quantum sensor networks in the simultaneous estimation of multiple properties of distributed signals.

-
- [1] Fadel, M., Yadin, B., Mao, Y., Byrnes, T. & Gessner, M. Multiparameter quantum metrology and mode entanglement with spatially split nonclassical spin ensembles. *New J. Phys.* **25**, 073006 (2023).
- [2] Giuseppe, G. D. & Vitali, D. Entangled light enhances force sensing. *Nat. Photonics* **17**, 465–466 (2023).
- [3] Xia, Y. *et al.* Entanglement-enhanced optomechanical sensing. *Nat. Photonics* **17**, 470–477 (2023).
- [4] Assouly, R., Dassonneville, R., Peronnin, T., Bienfait, A. & Huard, B. Quantum advantage in microwave quantum radar. *Nat. Phys.* (2023).
- [5] Crawford, S. E. *et al.* Quantum sensing for energy applications: Review and perspective. *Adv. Quantum Technol.* **4**, 2100049 (2021).
- [6] Cimini, V. *et al.* Experimental metrology beyond the standard quantum limit for a wide resources range. *npj Quantum Inf.* **9**, 20 (2023).
- [7] Yu, X. *et al.* Toward heisenberg scaling in non-hermitian metrology at the quantum regime. *Sci. Adv.* **10** (2024).
- [8] Sekatski, P., Wölk, S. & Dür, W. Optimal distributed sensing in noisy environments. *Phys. Rev. Res.* **2**, 023052 (2020).
- [9] Zhang, Z. & Zhuang, Q. Distributed quantum sensing. *Quantum Sci. Technol.* **6**, 043001 (2021).
- [10] Oh, C., Jiang, L. & Lee, C. Distributed quantum phase sensing for arbitrary positive and negative weights. *Phys. Rev. Res.* **4**, 023164 (2022).
- [11] Gündoğan, M. *et al.* Proposal for space-borne quantum memories for global quantum networking. *npj Quantum Inf.* **7** (2021).
- [12] Proctor, T. J., Knott, P. A. & Dunningham, J. A. Multiparameter estimation in networked quantum sensors. *Phys. Rev. Lett.* **120**, 080501 (2018).
- [13] Zhuang, Q., Preskill, J. & Jiang, L. Distributed quantum sensing enhanced by continuous-variable error correction. *New J. Phys.* **22**, 022001 (2020).
- [14] Nehra, R., Oh, C., Jiang, L. & Marandi, A. All-optical loss-tolerant distributed quantum sensing. *arXiv preprint arXiv:2407.13654* (2024).
- [15] Bringewatt, J., Bienias, P., Timothy, Q., Boettcher, I. & Gorshkov, A. Systems and methods for measurement of field properties using quantum sensor networks (2023). US Patent App. 17/978,420.
- [16] Yang, Y., Yadin, B. & Xu, Z.-P. Quantum-enhanced metrology with network states. *Phys. Rev. Lett.* **132**, 210801 (2024).
- [17] Marra, G. *et al.* Ultrastable laser interferometry for earthquake detection with terrestrial and submarine cables. *Science* **361**, 486–490 (2018).
- [18] Schnabel, R., Mavalvala, N., McClelland, D. E. & Lam, P. K. Quantum metrology for gravitational wave astronomy. *Nat. Commun.* **1**, 121 (2010).
- [19] Giovannetti, V., Lloyd, S. & Maccone, L. Quantum-enhanced positioning and clock synchronization. *Nature* **412**, 417–419 (2001).
- [20] Kómár, P. *et al.* A quantum network of clocks. *Nat. Phys.* **10**, 582–587 (2014).
- [21] Gendra, B., Calsamiglia, J., Muñoz Tapia, R., Bagan, E. & Chiribella, G. Probabilistic metrology attains macroscopic cloning of quantum clocks. *Phys. Rev. Lett.* **113**, 260402 (2014).
- [22] Grotti, J. *et al.* Geodesy and metrology with a transportable optical clock. *Nat. Phys.* **14**, 437–441 (2018).
- [23] Krutyanskiy, V. *et al.* Entanglement of trapped-ion qubits separated by 230 meters. *Phys. Rev. Lett.* **130**, 050803 (2023).
- [24] Bugalho, L., Coutinho, B. C., Monteiro, F. A. & Omar, Y. Distributing multipartite entanglement over noisy quantum networks. *Quantum* **7**, 920 (2023).
- [25] Knaut, C. M. *et al.* Entanglement of nanophotonic quantum memory nodes in a telecom network. *Nature* **629**, 573–578 (2024).
- [26] Ye, G.-S. *et al.* A photonic entanglement filter with rydberg atoms. *Nat. Photonics* **17**, 538–543 (2023).
- [27] Cao, A. *et al.* Multi-qubit gates and schrödinger cat states in an optical clock. *Nature* **634**, 315–320 (2024).
- [28] Liu, B. *et al.* Experimental adaptive bayesian estimation for a linear function of distributed phases in photonic

- quantum networks. *Optica* **11**, 1419 (2024).
- [29] Liu, L.-Z. *et al.* Distributed quantum phase estimation with entangled photons. *Nat. Photonics* **15**, 137–142 (2020).
- [30] Xia, Y. *et al.* Demonstration of a reconfigurable entangled radio-frequency photonic sensor network. *Phys. Rev. Lett.* **124**, 150502 (2020).
- [31] Liu, J.-L. *et al.* Creation of memory–memory entanglement in a metropolitan quantum network. *Nature* **629**, 579–585 (2024).
- [32] Liu, Q. *et al.* Nonlinear interferometry beyond classical limit enabled by cyclic dynamics. *Nat. Phys.* **18**, 167–171 (2021).
- [33] Malia, B. K., Wu, Y., Martínez-Rincón, J. & Kasevich, M. A. Distributed quantum sensing with mode-entangled spin-squeezed atomic states. *Nature* **612**, 661–665 (2022).
- [34] Li, S. *et al.* Ultrahigh-precision hamiltonian parameter estimation in a superconducting circuit. *Phys. Rev. Lett.* **132**, 250204 (2024).
- [35] Deng, X. *et al.* Quantum-enhanced metrology with large fock states. *Nat. Phys.* (2024).
- [36] Wang, W. *et al.* Heisenberg-limited single-mode quantum metrology in a superconducting circuit. *Nat. Commun.* **10** (2019).
- [37] Dixit, A. V. *et al.* Searching for dark matter with a superconducting qubit. *Phys. Rev. Lett.* **126**, 141302 (2021).
- [38] Tang, Z. *et al.* First scan search for dark photon dark matter with a tunable superconducting radio-frequency cavity. *Phys. Rev. Lett.* **133**, 021005 (2024).
- [39] Kang, R. *et al.* Near-quantum-limited haloscope search for dark-photon dark matter enhanced by a high-q superconducting cavity. *Phys. Rev. D* **109**, 095037 (2024).
- [40] Agrawal, A. *et al.* Stimulated emission of signal photons from dark matter waves. *Phys. Rev. Lett.* **132**, 140801 (2024).
- [41] Kurpiers, P. *et al.* Deterministic quantum state transfer and remote entanglement using microwave photons. *Nature* **558**, 264–267 (2018).
- [42] Axline, C. J. *et al.* On-demand quantum state transfer and entanglement between remote microwave cavity memories. *Nat. Phys.* **14**, 705–710 (2018).
- [43] Campagne-Ibarcq, P. *et al.* Deterministic remote entanglement of superconducting circuits through microwave two-photon transitions. *Phys. Rev. Lett.* **120**, 200501 (2018).
- [44] Leung, N. *et al.* Deterministic bidirectional communication and remote entanglement generation between superconducting qubits. *npj Quantum Inf.* **5** (2019).
- [45] Magnard, P. *et al.* Microwave quantum link between superconducting circuits housed in spatially separated cryogenic systems. *Phys. Rev. Lett.* **125**, 260502 (2020).
- [46] Zhong, Y. *et al.* Deterministic multi-qubit entanglement in a quantum network. *Nature* **590**, 571–575 (2021).
- [47] Burkhardt, L. D. *et al.* Error-detected state transfer and entanglement in a superconducting quantum network. *PRX Quantum* **2**, 030321 (2021).
- [48] Carrera Vazquez, A. *et al.* Combining quantum processors with real-time classical communication. *Nature* **636**, 75–79 (2024).
- [49] Niu, J. *et al.* Low-loss interconnects for modular superconducting quantum processors. *Nat. Electron.* **6**, 235–241 (2023).
- [50] Zhang, S. *et al.* Quantum-memory-enhanced preparation of nonlocal graph states. *Phys. Rev. Lett.* **128**, 080501 (2022).
- [51] Hoch, F. *et al.* Modular quantum-to-quantum bernoulli factory in an integrated photonic processor. *Nat. Photonics* (2024).
- [52] Zhou, S., Zhang, M., Preskill, J. & Jiang, L. Achieving the heisenberg limit in quantum metrology using quantum error correction. *Nat. Commun.* **9** (2018).
- [53] Cai, W. *et al.* Protecting entanglement between logical qubits via quantum error correction. *Nat. Phys.* **20**, 1022–1026 (2024).
- [54] Kim, D.-H. *et al.* Distributed quantum sensing of multiple phases with fewer photons. *Nat. Commun.* **15** (2024).
- [55] Mukhopadhyay, C. & Bayat, A. Modular many-body quantum sensors. *Phys. Rev. Lett.* **133**, 120601 (2024).
- [56] Hou, Z. *et al.* Zero-trade-off multiparameter quantum estimation via simultaneously saturating multiple heisenberg uncertainty relations. *Sci. Adv.* **7**, eabd2986 (2021).
- [57] Yuan, H. Sequential feedback scheme outperforms the parallel scheme for hamiltonian parameter estimation. *Phys. Rev. Lett.* **117**, 160801 (2016).
- [58] Hou, Z. *et al.* Control-enhanced sequential scheme for general quantum parameter estimation at the heisenberg limit. *Phys. Rev. Lett.* **123**, 040501 (2019).
- [59] Hou, Z. *et al.* Minimal tradeoff and ultimate precision limit of multiparameter quantum magnetometry under the parallel scheme. *Phys. Rev. Lett.* **125**, 020501 (2020).
- [60] Liu, Q., Hu, Z., Yuan, H. & Yang, Y. Optimal strategies of quantum metrology with a strict hierarchy. *Phys. Rev. Lett.* **130**, 070803 (2023).
- [61] Yang, X., Chen, X., Li, J., Peng, X. & Laflamme, R. Hybrid quantum-classical approach to enhanced quantum metrology. *Sci. Rep.* **11** (2021).
- [62] Kaubruegger, R. *et al.* Variational spin-squeezing algorithms on programmable quantum sensors. *Phys. Rev. Lett.* **123**, 260505 (2019).
- [63] Marciniak, C. D. *et al.* Optimal metrology with programmable quantum sensors. *Nature* **603**, 604–609 (2022).
- [64] Clausen, H. G., Rouchon, P. & Wisniewski, R. Online parameter estimation for continuously monitored quantum systems. *IEEE Control Syst. Lett.* **8**, 1247–1252 (2024).

Methods

Experimental platform

We implement this distributed quantum sensor on a superconducting quantum network consisting of five modules⁴⁹. In this setup, we design capacitive couplings among qubits on each module, while the communication across different modules is implemented via high-fidelity quantum state transfer through a microwave cable. The probe states are generated through a combination of quantum state transfer operations, local CNOT gates, and single-qubit rotations. The vector field signal and control units are digitally simulated and encoded using $U(3)$ formalism (also see Supplementary Information Section II.B), with signal parameters selected based on theoretical calculations, and control parameters determined by prior experimental knowledge. To extract signal information, Bell measurements are performed on the corresponding qubits, transforming the encoded state into probability distributions. The multiple components of the magnetic field parameters are then estimated from the Bell probabilities using MLE.

Maximum likelihood estimation and likelihood function benchmark

After measuring a set of Bell probability distributions, $\{P_i^{\text{exp}}\}$ for a specific signal parameter vector to be estimated and control parameter vector, we perform MLE to determine the signal parameters. In the MLE process, gradient optimization is employed to maximize the likelihood function $\mathcal{L} = \sum_i P_i^{\text{exp}} \ln(P_i^{\text{ideal}}(\hat{x}, \hat{x}_c))$ by varying the guess parameter \hat{x} and calculating the corresponding ideal probabilities. Here, P_i^{exp} and P_i^{ideal} represent the experimentally measured and numerically simulated probabilities for the i^{th} measurement basis state, respectively. The estimated parameters are expressed as $\hat{x}_{\text{est}} = \arg \max_{\hat{x}} \mathcal{L}(\hat{x}, \hat{x}_c)$.

Understanding the behavior of the likelihood function is essential for accurate MLE-based parameter estimation. To characterize the properties of \mathcal{L} near the true signal parameter values, we conduct an experimental benchmark of the likelihood function. This involves varying the guess parameters \hat{x} to measure the corresponding probabilities $\{P_i^{\text{exp}}(\hat{x}, \hat{x}_c)\}$ in experiment, while keeping the control parameters fixed to their optimal values. By comparing these probabilities to those measured at the true signal parameter values, $\{P_i^{\text{exp}}\}$, we construct the experimental likelihood function $\mathcal{L}' = \sum_i P_i^{\text{exp}} \ln(P_i^{\text{exp}}(\hat{x}, \hat{x}_c))$. The 2D landscapes of the normalized \mathcal{L}' as a function of the guess parameters are illustrated in Fig. 2d and Fig. 3b. This visualization reveals the parameter estimation space, characterized by an internal boundary whose saddle point corresponds to the alignment of the guess parameters with the true signal parameters. Additionally, the shrinking of the internal boundary with increasing cycles N indicates enhanced precision achieved

through the sequential strategy. Our experimentally probed landscapes align closely with numerical simulations, which validates the MLE approach based solely on experimental measurements and paves the way for advancing towards a programmable sensor system that relies only on experimental measurements and parameter update feedback.

Adaptive control-enhanced sensing protocol

We conduct an adaptive strategy to search for the optimal control parameters^{61–63}. This part is realized in four steps. Step one, we randomly guess a set of control parameters $\hat{x}_c^{(0)} = (B_c^{(0)}, \theta_c^{(0)}, \phi_c^{(0)})$, conduct the sensing circuit and obtain probability distribution $\{P_i^{\text{exp}(0)}\}$. Step two, the maximum-likelihood estimation gives the first estimation of unknown parameters, $\hat{x}_{\text{est}}^{(1)} = \arg \max_{\hat{x}} \sum_i P_i^{\text{exp}(0)} \ln(P_i^{\text{ideal}}(\hat{x}, \hat{x}_c^{(0)}))$. This set of estimator updates the control parameters $\hat{x}_c^{(1)} = \hat{x}_{\text{est}}^{(1)}$. Step three, we update the control parameters with $\hat{x}_c^{(1)}$ and repeat the experiment, obtain probability distribution $\{P_i^{\text{exp}(1)}\}$. Step four, by the maximum-likelihood function, we update the estimators as well as the control parameters with all previous results as $\hat{x}_c^{(2)} = \hat{x}_{\text{est}}^{(2)} = \arg \max_{\hat{x}} \sum_i P_i^{\text{exp}(0)} \ln(P_i^{\text{ideal}}(\hat{x}, \hat{x}_c^{(0)})) \times \sum_i P_i^{\text{exp}(1)} \ln(P_i^{\text{ideal}}(\hat{x}, \hat{x}_c^{(1)}))$. Repeat the above adaptive process for K times, we get the estimators $\hat{x}_{\text{est}}^{(K)} = \arg \max_{\hat{x}} \mathcal{L}_{\text{joint}}$,

where $\mathcal{L}_{\text{joint}} = \prod_{m=1}^{K-1} \sum_i P_i^{\text{exp}(m)} \ln[P_i^{\text{ideal}}(\hat{x}, \hat{x}_c^{(m)})]$ is the joint likelihood function⁶⁴. The K -th MLE considers all $K-1$ experiment results, the control parameters will be updated with the increasing of iteration cycles. After at most $R_{\text{iter}} = 40$ rounds, the iteration result, namely the estimator $B_{\text{est}}, \theta_{\text{est}}$ and ϕ_{est} converge to the optimal parameters.

We demonstrate the convergence of the adaptive protocol in Extended Data Fig. 1 by minimizing the joint likelihood function $-\mathcal{L}_{\text{joint}}$ in each cycle and tracking the evolution of the cost function $(-1)^{R_{\text{iter}}} \times \mathcal{L}_{\text{joint}}$. The convergence process is shown to be robust both across various initial guesses at $N = 1$ and across sequential copies ($N = 1$ to 6) for a fixed initial guess, as depicted in Extended Data Fig. 1a,b. Numerical analysis of the joint likelihood function at $N = 4$ (Extended Data Fig. 1c) indicates that, while the landscape initially appears irregular, it evolves into an optimal configuration similar to that in Fig. 2b after a few cycles, highlighting the effectiveness of this optimization process.

Ultimate precision for remote vector field sensing

The Hamiltonian for the sensor qubit can be expressed in spherical coordinates as $H = \vec{B} \cdot \sigma$, where the vector field $\vec{B} = (B_x, B_y, B_z)$ is defined in terms of its spherical components $B_x = B \sin \theta \cos \phi$, $B_y = B \sin \theta \sin \phi$, and $B_z = B \cos \theta$. During the free evolution of the Hamiltonian over the encoding time T , the unitary operator describing the system is $U_s(\hat{x}) = e^{-i\vec{B} \cdot \sigma T}$, with $\hat{x} = (B, \theta, \phi)$.

To evaluate the performance of a sensing strategy, we utilize the quantum Cramér-Rao bound, which is expressed as $n \text{Cov}(\hat{x}) \geq F_Q^{-1}$, where $\text{Cov}(\hat{x})$ is the covariance matrix of the estimators corresponding to the unknown parameters \hat{x} , n is the number of measurement repetitions, and F_Q is the quantum Fisher information matrix

(QFIM). The estimation precision for multiple parameters is quantified by the sum of variances ($\text{Tr}[\text{Cov}(\hat{x})]$). To achieve better estimation precision, we apply the control-enhanced sequential scheme, insert the control operation U_c after each signal unitaries U_s and repeat the cycle N times^{56–60}. Under the optimal strategy, we

have $F_Q^{\max} = 4N^2 \begin{pmatrix} T^2 & 0 & 0 \\ 0 & \sin^2(BT) & 0 \\ 0 & 0 & \sin^2(BT)\sin^2\theta \end{pmatrix}$. In

this case, the quantum Cramer-Rao bound is achievable (see Supplementary Information Section I.B for derivation). The ultimate precision limit for the estimation of the three parameters is then $n\delta B_{\text{est}}^2 \geq (4N^2 T^2)^{-1}$, $n\delta\theta_{\text{est}}^2 \geq (4N^2 \sin^2(BT))^{-1}$ and $n\delta\phi_{\text{est}}^2 \geq (4N^2 \sin^2(BT)\sin^2\theta)^{-1}$. For each of the parameters, this is also the highest precision that can be achieved in the single-parameter case where the other two parameters are taken as known values. The optimal strategy thus achieves the highest precision for all three parameters simultaneously without any tradeoff.

Precision limit for gradient estimation with non-local entanglement

Under the optimal controlled sequential scheme, the total dynamics is given by $(U_S U_C)^N$, where $U_S(\hat{x}) = U_{s1}^{\otimes 2} \otimes U_{s2}^{\otimes 2}$, $U_C = U_S^\dagger(\hat{x}_c)$ with $\hat{x}_c = (\nabla \vec{B}_c, \sum \vec{B}_c)$ ^{56,57}. As detailed in the Supplementary Information Section I.C.1, using a non-local entangled probe state $|\Psi_0\rangle$, the QFIM for the simultaneous estimation of $\hat{x} = (\nabla \vec{B}, \sum \vec{B})$ is given by $F_Q = N^2 \begin{pmatrix} F_- & \mathbf{0} \\ \mathbf{0} & F_+ \end{pmatrix}$, where F_- and F_+ correspond to the QFIMs for estimating $\nabla \vec{B}$ and $\sum \vec{B}$, respectively. The optimal measurement that saturates the QCRB is the local projective measurement in the Bell basis at each location. The block diagonal form of the QFIM implies that estimating the sum vector $\sum \vec{B}$ does not affect the precision of estimating the gradients $\nabla \vec{B}$. For benchmarking, we assess our estimation protocol's performance at zero-gradient. Specifically, for the estimation of ∇B_x and ∇B_y of two-dimensional vector fields, we have

$$\begin{aligned} & (\delta \nabla B_{x_{\text{est}}})^2 + (\delta \nabla B_{y_{\text{est}}})^2 \\ & \geq \frac{1}{4N^2} \left(\frac{1}{T^2} + \frac{B^2}{(1 + 3\sin^2(BT))\sin^2(BT)} \right), \end{aligned} \quad (1)$$

where B is the magnitude of the vector field with $B = \sqrt{B_x^2 + B_y^2 + B_z^2}$. This demonstrates the Heisenberg scaling (See Supplementary Information Section I.C.1 for the analysis of three-dimensional case).

Precision limit for gradient estimation with local entanglement

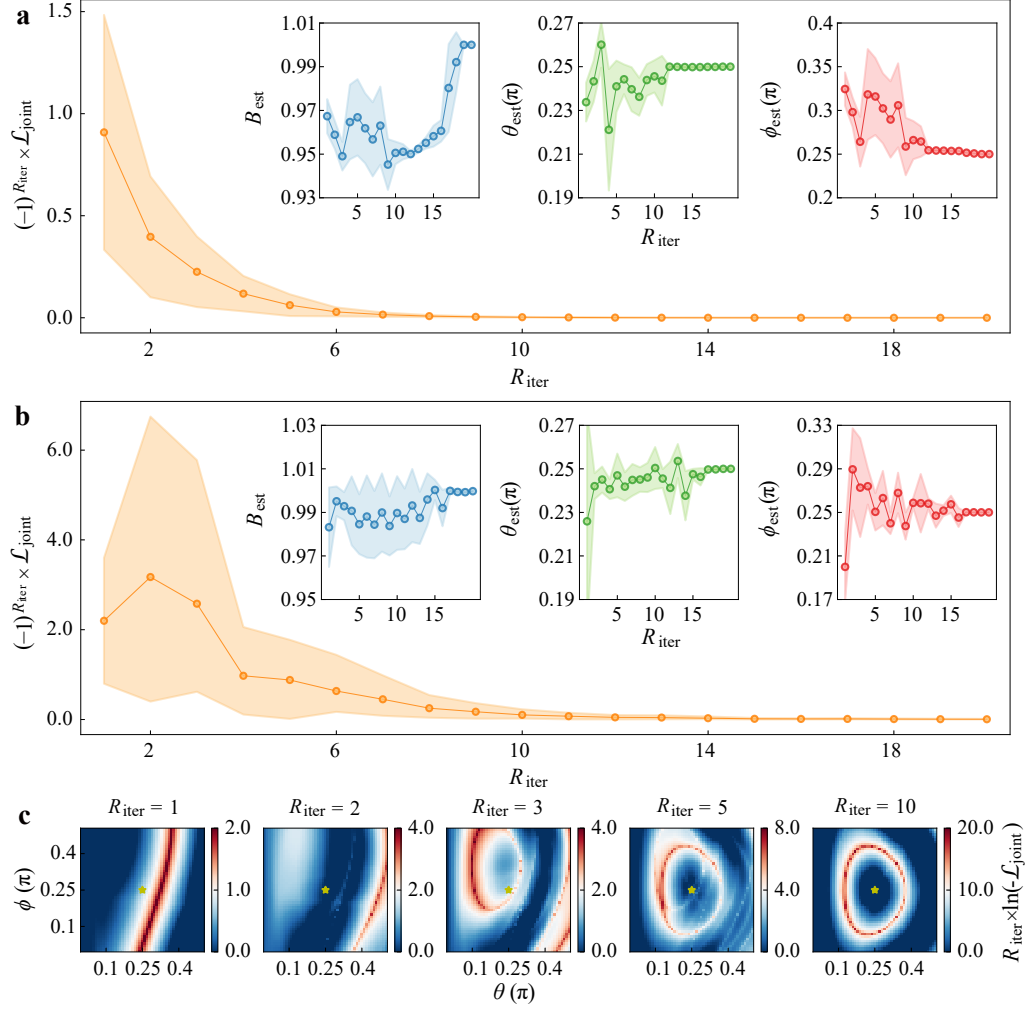
We theoretically determine the precision limits for the estimation of the gradients under the local strategy. Under the optimal strategy, the ultimate precision for estimating ∇B_x and ∇B_y of two-dimensional vector fields is

$$(\delta \nabla B_{x_{\text{est}}})^2 + (\delta \nabla B_{y_{\text{est}}})^2 \geq \frac{1}{8N^2} \left(\frac{1}{T^2} + \frac{B^2}{\sin^2(BT)} \right). \quad (2)$$

The optimal probe state achieving the ultimate precision depends on the true values of the parameter and thus requires adaptive preparation. For practical purposes, we use the Bell state $\frac{1}{\sqrt{2}}(|00\rangle + |11\rangle)$, which is parameter-independent and does not require adaptive preparation. In this case, the precision is

$$\begin{aligned} & (\delta \nabla B_{x_{\text{est}}})^2 + (\delta \nabla B_{y_{\text{est}}})^2 \\ & \geq \frac{1}{8N^2 \sin^2(BT)} \left(\frac{B^2 - \cos^2(BT)B_x^2}{T^2 B_x^2} + \frac{B^2}{\sin^2(BT)} \right). \end{aligned} \quad (3)$$

When $B_x = B_y$, as we considered in the experiment, the two bounds become almost the same near the optimal time point with $\sin(BT) = 1$. More details can be found in Section I.C.2 of Supplementary.



Extended Data Fig. 1. **Adaptive control-enhanced metrology for simultaneous three-parameter estimation with signal parameters $(B, \theta, \phi) = (1, \frac{\pi}{4}, \frac{\pi}{4})$.** **a**, The results of adaptive iterations starting from different initial guess values (10 sets randomly chosen within the boundary of the landscape) with $N = 1$. **b**, The results of adaptive iterations with different sequential copies $N = 1$ to 6 and fixed initial guess (1 set randomly chosen within the boundary of the landscape for $N = 1$). **c**, The calculated likelihood function landscape for $N = 4$ after iteration cycle 1, 2, 3, 5, 10. Stars indicate the locations of the optimal control parameters.

Acknowledgements

We thank Xiu-Hao Deng, Zhibo Hou and Raphael Kaubruegger for insightful discussions. This work was supported by the National Natural Science Foundation of China (12174178 and 12374474), the Science, Technology and Innovation Commission of Shenzhen Municipality (KQTD20210811090049034, RCBS20231211090824040, RCBS20231211090815032), the Shenzhen-Hong Kong Cooperation Zone for Technology and Innovation (HZQB-KCZYB-2020050), Guangdong Basic and Applied Basic Research Foundation (2024A1515011714, 2022A1515110615), Research Grants Council of Hong Kong with Grants No. 14309223, No. 14309624, No. 14309022, the Innovation Program for Quantum Science and Technology (Grant No. 2023ZD0300600), and the Guangdong Provincial Quantum Science Strategic Initiative (Grant No. GDZX2303007).

Author contributions

Jiajian Z. conducted the measurements and analyzed the data with Y.-J.H. under the supervision of J.N. L.W.

and Y.-J.H. provided theoretical support guided by H.Y. Jiawei Z. developed the microwave electronics infrastructure. Y.Z supervised the project. All authors contributed to the discussions and the writing of the manuscript.

Competing interests

The authors declare no competing interests.

Data availability

The data that support the plots within this paper and other findings of this study are available from the corresponding author upon reasonable request.

Supplementary Information for “Distributed multi-parameter quantum metrology with a superconducting quantum network”

CONTENTS

I. Theoretical analysis	2
A. General process of quantum metrology	2
B. Sensing of a remote vector field	3
C. Sensing of the gradients between vector fields	5
1. Non-local entanglement	5
2. Local entanglement	9
3. Strategy comparison	13
II. Experimental implementation	17
A. Device information	17
B. Gate performance	19
C. Implementation of distributed sensing in quantum circuits	19
III. Extended data	23
A. Extended data for sensing of remote vector fields	23
B. Extended data for distributed sensing of vector field gradient	24
C. The influence of noise	25
References	28

I. THEORETICAL ANALYSIS

A. General process of quantum metrology

The primary objective of quantum metrology is to precisely estimate unknown physical quantities by utilizing quantum resources, such as quantum entanglement. The general process of quantum metrology includes the following steps: state preparation, parameter encoding, measurement, and estimation. The probe state ρ_0 evolves under the given dynamics, which depend on the unknown parameters $\hat{x} = (x_1, \dots, x_n)$, resulting in the encoded state $\rho(\hat{x})$. To extract information about the parameters \hat{x} , we perform a set of positive operator-valued measures (POVMs), represented as $\{\Pi_i\}$, on the state $\rho(\hat{x})$, obtaining a set of probability distributions $P_i(\hat{x})$, where $P_i(\hat{x})$ is the probability of obtaining the measurement result i . Finally, we construct the estimators $\hat{x}_{\text{est}} = (x_{1\text{est}}, \dots, x_{n\text{est}})$ based on the probabilities of the measurement outcomes. For multi-parameter quantum estimating, the performance of locally unbiased estimators is quantified by the covariance matrix, where the jk -th element gives

$$[\text{Cov}(\hat{x})]_{jk} = E[(x_{j\text{est}} - x_j)(x_{k\text{est}} - x_k)]. \quad (\text{S1})$$

The estimation precision for multiple parameters is quantified by the sum of variances, which corresponds to the sum of the diagonal terms of the covariance matrix. The covariance matrix is lower bounded by

$$\text{Cov}(\hat{x}) \geq \frac{1}{n} F_C^{-1} \quad (\text{S2})$$

which is known as the Cramér-Rao bound. Here n is the number of measurement repetitions, and F_C is the Fisher information matrix (FIM) with jk -th element calculated as follows:

$$[F_C]_{x_j x_k} = \sum_i \frac{1}{P_i(\hat{x})} \left(\frac{\partial P_i(\hat{x})}{\partial x_j} \right) \left(\frac{\partial P_i(\hat{x})}{\partial x_k} \right) \quad (\text{S3})$$

The Cramér-Rao bound is achievable for a large number of repetitions by using the maximum likelihood estimator (MLE). The quantum Cramér-Rao bound (QCRB) further constrains the covariance matrix:

$$\text{Cov}(\hat{x}) \geq \frac{1}{n} F_C^{-1} \geq \frac{1}{n} F_Q^{-1}. \quad (\text{S4})$$

Here F_Q is the quantum Fisher information matrix (QFIM). For parameters encoded in pure states $|\psi_{\hat{x}}\rangle$, F_Q can be expressed as:

$$[F_Q]_{x_j x_k} = 4 \text{Re}(\langle \partial_j \psi_{\hat{x}} | \partial_k \psi_{\hat{x}} \rangle - \langle \partial_j \psi_{\hat{x}} | \psi_{\hat{x}} \rangle \langle \psi_{\hat{x}} | \partial_k \psi_{\hat{x}} \rangle). \quad (\text{S5})$$

More specifically, consider a pure probe state $|\psi_0\rangle$ undergoes a unitary process $U_{\hat{x}}$, the encoded state $|\psi_{\hat{x}}\rangle = U_{\hat{x}}|\psi_0\rangle$. Define the generator of $U_{\hat{x}}$ corresponding to unknown parameter x_j as

$$h_{x_j} = iU_{\hat{x}}^\dagger (\partial_{x_j} U_{\hat{x}}). \quad (\text{S6})$$

Then, the quantum Fisher information matrix in Eq.(S5) can be expressed in terms of the generators,

$$[F_Q]_{x_j x_k} = 2\langle \psi_0 | \{h_{x_j}, h_{x_k}\} | \psi_0 \rangle - 4\langle \psi_0 | h_{x_j} | \psi_0 \rangle \langle \psi_0 | h_{x_k} | \psi_0 \rangle. \quad (\text{S7})$$

Here $\{\cdot, \cdot\}$ denotes the anti-commutator. According to QCRB, the precision of estimating multiple parameters is lower bound by $n\text{Tr}(\text{Cov}(\hat{x})) \geq \text{Tr}(F_C^{-1}) \geq \text{Tr}(F_Q^{-1})$. Hence, finding the maximal QFIM and the optimal measurement that saturates the QCRB leads to the ultimate precision of estimation. For multi-parameter quantum estimation, the necessary and sufficient condition for saturating the quantum Cramér-Rao bound in pure states is the weak commutativity condition, which is

$$\text{Im} [\langle \partial_{x_j} \psi_{\hat{x}} | \partial_{x_k} \psi_{\hat{x}} \rangle] = 0, \forall x_j, x_k. \quad (\text{S8})$$

To achieve the best precision for estimating unknown parameters \hat{x} , it is crucial to optimize every step of the process. This includes optimizing the initial state, adding additional controls, and performing the optimal measurement that saturates the quantum Cramér-Rao bound. In the control-enhanced sequential scheme, the total system evolution is described by $U_N = (U_c U_{\hat{x}})^N$, where $U_{\hat{x}}$ represents the system dynamics over encoding time T , and U_c denotes the control applied after each encoding time T . The optimal control strategy involves selecting $U_c = U_{\hat{x}}^\dagger$, as derived in [1]. With the implementation of N cycles of optimal control, the quantum Fisher information matrix becomes $N^2 F_Q$, reaching the Heisenberg limit. Here, F_Q denotes the QFIM for $N = 1$ without control, as adding only one control at the end of evolution cannot change the QFIM. To streamline the analysis, we examine the (maximal) QFIM for sensing strategies without control in the following sections. For cases with optimal control, the QFIM can be obtained by multiplying by N^2 .

B. Sensing of a remote vector field

We consider the estimation of three components of a remote vector field, described in spherical coordinates (B, θ, ϕ) as $\vec{B} = (B \sin \theta \cos \phi, B \sin \theta \sin \phi, B \cos \theta)$, instead of in Cartesian coordinates $\vec{B} = (B_x, B_y, B_z)$. Estimating the vector field components $\vec{B} = (B_x, B_y, B_z)$ thus corresponds to simultaneously estimating the parameters $\hat{x} = (B, \theta, \phi)$. For each sensor qubit at time T , the evolution can be represented by $U_s = e^{-i\vec{B} \cdot \sigma T} = e^{-iBT \mathbf{n} \cdot \sigma}$ with $\mathbf{n} = (\sin \theta \cos \phi, \sin \theta \sin \phi, \cos \theta)$. The generator for $x_j \in \{B, \theta, \phi\}$ is given by

$$\begin{aligned} h_B &= c_B \mathbf{n}_B \cdot \sigma \\ h_\theta &= c_\theta \mathbf{n}_\theta \cdot \sigma \\ h_\phi &= c_\phi \mathbf{n}_\phi \cdot \sigma \end{aligned} \quad (\text{S9})$$

with

$$c_B = T, \quad c_\theta = \sin(BT), \quad c_\phi = \sin(BT) \sin \theta \quad (\text{S10})$$

$$\begin{aligned} \mathbf{n}_B &= \mathbf{n} = (\sin \theta \cos \phi, \sin \theta \sin \phi, \cos \theta) \\ \mathbf{n}_\theta &= \cos(BT) \mathbf{n}_1 - \sin(BT) \mathbf{n}_2 \\ \mathbf{n}_\phi &= \sin(BT) \mathbf{n}_1 + \cos(BT) \mathbf{n}_2 \end{aligned} \quad (\text{S11})$$

where $\mathbf{n}_1 = \partial_\theta \mathbf{n} = (\cos \theta \cos \phi, \cos \theta \sin \phi, -\sin \theta)$, $\mathbf{n}_2 = \mathbf{n} \times \mathbf{n}_1 = (-\sin \phi, \cos \phi, 0)$. It is easy to verify that \mathbf{n} , \mathbf{n}_1 , \mathbf{n}_2 are orthogonal to each other. There exists a unitary transformation $U_r = e^{i\frac{BT}{2}\mathbf{n}\cdot\boldsymbol{\sigma}} e^{-i\frac{\phi}{2}\sigma_z} e^{-i\frac{\theta}{2}\sigma_y}$ such that

$$\mathbf{n}_B \cdot \boldsymbol{\sigma} = U_r \sigma_z U_r^\dagger, \quad \mathbf{n}_\theta \cdot \boldsymbol{\sigma} = U_r \sigma_x U_r^\dagger, \quad \mathbf{n}_\phi \cdot \boldsymbol{\sigma} = U_r \sigma_y U_r^\dagger, \quad (\text{S12})$$

Assume the initial probe state is $|\psi_{SA}\rangle$, where the ancilla system is introduced. Then using Eq.(S7), we obtain the QFIM as

$$F_Q = 4 \begin{pmatrix} T^2 - (\text{Tr}(\rho_S h_B))^2 & -\text{Tr}(\rho_S h_B) \text{Tr}(\rho_S h_\theta) & -\text{Tr}(\rho_S h_B) \text{Tr}(\rho_S h_\phi) \\ -\text{Tr}(\rho_S h_B) \text{Tr}(\rho_S h_\theta) & \sin^2(BT) - (\text{Tr}(\rho_S h_\theta))^2 & -\text{Tr}(\rho_S h_\theta) \text{Tr}(\rho_S h_\phi) \\ -\text{Tr}(\rho_S h_B) \text{Tr}(\rho_S h_\phi) & -\text{Tr}(\rho_S h_\theta) \text{Tr}(\rho_S h_\phi) & \sin^2(BT) \sin^2 \theta - (\text{Tr}(\rho_S h_\theta))^2 \end{pmatrix} \quad (\text{S13})$$

where $\rho_S = \text{Tr}_A(|\psi_{SA}\rangle\langle\psi_{SA}|)$ denotes the reduced state by tracing out the ancilla system. The maximal QFIM, denoted as F_Q^{\max} , is

$$F_Q^{\max} = 4 \begin{pmatrix} T^2 & 0 & 0 \\ 0 & \sin^2(BT) & 0 \\ 0 & 0 & \sin^2(BT) \sin^2 \theta \end{pmatrix}. \quad (\text{S14})$$

F_Q^{\max} represents the upper limit of the QFIM under optimal conditions. This is because $F_Q^{\max} - F_Q$ is always a positive semi-definite matrix, a property that signifies no other state can yield a higher QFIM value. The maximal QFIM is achieved when choosing $\rho_S = \frac{1}{2}I$, indicating that the optimal initial state for maximizing the QFIM is a maximally entangled state, denoted as $|\psi_{SA}\rangle = \frac{1}{\sqrt{2}}(|00\rangle + |11\rangle)$. The projective measurement in the Bell basis is the optimal measurement that saturates the quantum Cramér-Rao bound, which is given as

$$M_{00} = |\Phi^+\rangle\langle\Phi^+|, \quad M_{01} = |\Phi^-\rangle\langle\Phi^-|, \quad M_{10} = |\Psi^+\rangle\langle\Psi^+|, \quad M_{11} = |\Psi^-\rangle\langle\Psi^-|, \quad (\text{S15})$$

where the Bell states are given by:

$$\begin{aligned} |\Phi^+\rangle &= \frac{1}{\sqrt{2}}(|00\rangle + |11\rangle), & |\Phi^-\rangle &= \frac{1}{\sqrt{2}}(|00\rangle - |11\rangle), \\ |\Psi^+\rangle &= \frac{1}{\sqrt{2}}(|01\rangle + |10\rangle), & |\Psi^-\rangle &= \frac{1}{\sqrt{2}}(|01\rangle - |10\rangle). \end{aligned} \quad (\text{S16})$$

The probability of the measurement results in the Bell basis

$$\begin{aligned} P_{00} &= \text{Tr}(\rho(B, \theta, \phi) M_{00}) = \cos^2(BT) \\ P_{01} &= \text{Tr}(\rho(B, \theta, \phi) M_{01}) = \sin^2(BT) \cos^2 \theta \\ P_{10} &= \text{Tr}(\rho(B, \theta, \phi) M_{10}) = \sin^2(BT) \sin^2 \theta \cos^2 \phi \\ P_{11} &= \text{Tr}(\rho(B, \theta, \phi) M_{11}) = \sin^2(BT) \sin^2 \theta \sin^2 \phi \end{aligned} \quad (\text{S17})$$

where $\rho(B, \theta, \phi) = (U_s \otimes I)|\psi_{SA}\rangle\langle\psi_{SA}|(U_s^\dagger \otimes I)$ is density matrix for the evolved state. Based on the probability distribution, by using Eq.(S3), it is straightforward to verify the classical Fisher information matrix equals the quantum Fisher information matrix, thereby saturating the quantum Cramér-Rao bound. The estimated precision limits for vector components are given by:

$$\delta B_{\text{est}}^2 \geq \frac{1}{4T^2}, \quad \delta \theta_{\text{est}}^2 \geq \frac{1}{4 \sin^2(BT)}, \quad \delta \phi_{\text{est}}^2 \geq \frac{1}{4 \sin^2(BT) \sin^2 \theta} \quad (\text{S18})$$

Following the error propagation formula, we calculate:

$$\begin{aligned}
\delta B_{x_{\text{est}}} &= \sin \theta \cos \phi \delta B_{\text{est}} + B \cos \theta \cos \phi \delta \theta_{\text{est}} - B \sin \theta \sin \phi \delta \phi_{\text{est}} \\
\delta B_{y_{\text{est}}} &= \sin \theta \sin \phi \delta B_{\text{est}} + B \cos \theta \sin \phi \delta \theta_{\text{est}} + B \sin \theta \cos \phi \delta \phi_{\text{est}} \\
\delta B_{z_{\text{est}}} &= \cos \theta \delta B_{\text{est}} - B \sin \theta \delta \theta_{\text{est}}
\end{aligned} \tag{S19}$$

The summation of squared deviations gives the precision limits for estimating three components of a vector field:

$$\begin{aligned}
\delta B_{x_{\text{est}}}^2 + \delta B_{y_{\text{est}}}^2 + \delta B_{z_{\text{est}}}^2 &= \delta B_{\text{est}}^2 + B^2 \delta \theta_{\text{est}}^2 + B^2 \sin^2 \theta \delta \phi_{\text{est}}^2 \\
&\geq \frac{1}{4T^2} + \frac{B^2}{2 \sin^2(BT)}.
\end{aligned} \tag{S20}$$

C. Sensing of the gradients between vector fields

In this section, we consider the estimation of the gradients between two remote vector fields, expressed as $\nabla \vec{B} = \vec{B}_1 - \vec{B}_2 = (\nabla B_x, \nabla B_y, \nabla B_z)$. For each sensor qubit, the Hamiltonian H_j is given by $H_j = \vec{B}_j \cdot \boldsymbol{\sigma} = B_{jx} \sigma_x + B_{jy} \sigma_y + B_{jz} \sigma_z$, where $\vec{B}_j = (B_{jx}, B_{jy}, B_{jz})$ represents the vector field components and $\boldsymbol{\sigma} = (\sigma_x, \sigma_y, \sigma_z)$ denotes the spin vector. Alternatively, in spherical coordinates, the Hamiltonian is represented as $H_j = B_j \mathbf{n}_j \cdot \boldsymbol{\sigma}$, where $\mathbf{n}_j = (\sin \theta_j \cos \phi_j, \sin \theta_j \sin \phi_j, \cos \theta_j)$ and $B_j = \sqrt{B_{jx}^2 + B_{jy}^2 + B_{jz}^2}$ represents the magnitude of the vector field. The evolution at time T can be represented by $U_{sj} = e^{-i\vec{B}_j \cdot \boldsymbol{\sigma} T} = e^{-iB_j \mathbf{n}_j \cdot \boldsymbol{\sigma} T}$ for $j = 1, 2$.

We evaluate the precision of two strategies for estimating vector field gradients. The first strategy employs non-local entanglement, directly estimating the vector field gradient by leveraging entanglement across the sensor network. The second uses local entanglement, measuring each vector field independently at the two locations and then calculating the gradient. Our comparison highlights the precision benefits of distributed quantum sensing, with non-local entanglement offering distinct advantages for accurate gradient estimation.

1. Non-local entanglement

Utilizing non-local entanglement enables the direct and simultaneous estimation of spatial gradients, potentially giving higher precision. In this approach, we introduce a 4-qubit non-local entangled state as the probe state, $|\Psi_0\rangle = \frac{1}{\sqrt{2}}(|0011\rangle - |1100\rangle)$, to directly estimate gradients along three directions. The first two qubits and the last two qubits are sent to two separate sensor modules (module \mathcal{B} and \mathcal{C} in the main text), respectively. The total evolution of the dynamics is expressed as $U_S = U_{s1} \otimes U_{s1} \otimes U_{s2} \otimes U_{s2}$, which gives the evolved state as $U_S |\Psi_0\rangle$, containing the information of the spatial gradients. Denote the sum of two vector fields as $\sum \vec{B} = \vec{B}_1 + \vec{B}_2 = (\sum B_x, \sum B_y, \sum B_z)$. The components of the vector field can then be rewritten as

$$B_{1p} = \frac{\sum B_p + \nabla B_p}{2}, \quad B_{2p} = \frac{\sum B_p - \nabla B_p}{2}, \quad \text{for } p \in \{x, y, z\}. \tag{S21}$$

To effectively estimate the gradients, denoted as $\nabla \vec{B}$, it is also necessary to acquire information about the sum of the vector fields, denoted here as $\sum \vec{B}$. This information is crucial for adaptively implementing control strategies. Such control strategies essentially reduce the problem of estimating general gradients $\nabla \vec{B}$ to estimating $\nabla \vec{B} = (0, 0, 0)$, indicating $\vec{B}_1 = \vec{B}_2 = \vec{B}$. This can be realized by adding compensation to the vector fields if the gradients are non-zero. Therefore, we benchmark the performance of our estimation protocol at zero-gradient, and the comparison of different strategies will also be made under this assumption.

Under the dynamics governed by U_S , the quantum Fisher information matrix for simultaneously estimating $\hat{x} = (\nabla \vec{B}, \sum \vec{B})$ is given by

$$F_Q = \begin{pmatrix} F_- & \mathbf{0} \\ \mathbf{0} & F_+ \end{pmatrix}, \quad (\text{S22})$$

where this matrix is block-diagonal, with F_- and F_+ representing the QFIM for estimating $\nabla \vec{B} = (\nabla B_x, \nabla B_y, \nabla B_z)$ and $\sum \vec{B} = (\sum B_x, \sum B_y, \sum B_z)$, respectively, which are given by

$$F_- = \begin{pmatrix} [F_Q]_{\nabla B_x \nabla B_x} & [F_Q]_{\nabla B_x \nabla B_y} & [F_Q]_{\nabla B_x \nabla B_z} \\ [F_Q]_{\nabla B_x \nabla B_y} & [F_Q]_{\nabla B_y \nabla B_y} & [F_Q]_{\nabla B_y \nabla B_z} \\ [F_Q]_{\nabla B_x \nabla B_z} & [F_Q]_{\nabla B_y \nabla B_z} & [F_Q]_{\nabla B_z \nabla B_z} \end{pmatrix}, \quad (\text{S23})$$

with

$$\begin{aligned} [F_Q]_{\nabla B_x \nabla B_x} &= \frac{4}{B^4} (B_x^2 T^2 (B^2 + 3B_z^2) + \sin^2(BT)(B_y^2 + B_z^2 + 6B_x B_y B_z T + 3B_y^2 \sin^2(BT))) \\ &\quad + \frac{3B_x B_z \sin(2BT)}{B^6} (-4BB_y \sin^2(BT) + B_x B_z (-4BT + \sin(2BT))), \\ [F_Q]_{\nabla B_y \nabla B_y} &= \frac{4}{B^4} (B_y^2 T^2 (B^2 + 3B_z^2) + \sin^2(BT)(B_x^2 + B_z^2 - 6B_x B_y B_z T + 3B_x^2 \sin^2(BT))) \\ &\quad + \frac{3B_y B_z \sin(2BT)}{B^6} (4BB_x \sin^2(BT) + B_y B_z (-4BT + \sin(2BT))), \\ [F_Q]_{\nabla B_z \nabla B_z} &= \frac{4}{B^4} (B_z^2 T^2 (B^2 + 3B_z^2) + \sin^2(BT)(B_x^2 + B_y^2)) \\ &\quad + \frac{3 \sin(2BT)}{B^6} (4B(B_x^2 + B_y^2) B_z T + (B_x^2 + B_y^2)^2 \sin(2BT)), \\ [F_Q]_{\nabla B_x \nabla B_y} &= \frac{4}{B^4} (B_x B_y T^2 (B^2 + 3B_z^2) - \sin^2(BT)(4B_x B_y + 3B_z T (B_x^2 - B_y^2))) \\ &\quad + \frac{3 \sin(2BT)}{B^6} (2BB_z \sin^2(BT)(B_x^2 - B_y^2) + B_x B_y (-4BB_z T + (B^2 + B_z^2) \sin(2BT))), \\ [F_Q]_{\nabla B_x \nabla B_z} &= \frac{4B_z}{B^4} (B_x T^2 (B^2 + 3B_z^2) - \sin^2(BT)(B_x - 3B_y B_z T)) \\ &\quad + \frac{3 \sin(2BT)}{B^6} (2BB_y \sin^2(BT)(B_x^2 + B_y^2) + B_x B_z (2BT(B^2 - 2B_z^2) - (B^2 - B_z^2) \sin(2BT))), \\ [F_Q]_{\nabla B_y \nabla B_z} &= \frac{4B_z}{B^4} (B_y T^2 (B^2 + 3B_z^2) - \sin^2(BT)(B_y + 3B_x B_z T)) \\ &\quad - \frac{3 \sin(2BT)}{B^6} (2BB_x \sin^2(BT)(B_x^2 + B_y^2) - B_y B_z (2BT(B^2 - 2B_z^2) - (B^2 - B_z^2) \sin(2BT))), \end{aligned} \quad (\text{S24})$$

and

$$F_+ = \begin{pmatrix} [F_Q]_{\sum B_x \sum B_x} & [F_Q]_{\sum B_x \sum B_y} & [F_Q]_{\sum B_x \sum B_z} \\ [F_Q]_{\sum B_x \sum B_y} & [F_Q]_{\sum B_y \sum B_y} & [F_Q]_{\sum B_y \sum B_z} \\ [F_Q]_{\sum B_x \sum B_z} & [F_Q]_{\sum B_y \sum B_z} & [F_Q]_{\sum B_z \sum B_z} \end{pmatrix}, \quad (\text{S25})$$

with

$$\begin{aligned}
[F_Q]_{\Sigma B_x \Sigma B_x} &= \frac{4}{B^4} (B_x^2 T^2 (B_x^2 + B_y^2) + B_z \sin^2(BT) (B_z - 2B_x B_y T)) \\
&\quad + \frac{\sin(2BT)}{B^6} (4BB_x^2 B_z^2 T + 4BB_x B_y B_z \sin^2(BT) + (B^2 B_y^2 - B_x^2 B_z^2) \sin(2BT)), \\
[F_Q]_{\Sigma B_y \Sigma B_y} &= \frac{4}{B^4} (B_y^2 T^2 (B_x^2 + B_y^2) + B_z \sin^2(BT) (B_z + 2B_x B_y T)) \\
&\quad + \frac{\sin(2BT)}{B^6} (4BB_y^2 B_z^2 T - 4BB_x B_y B_z \sin^2(BT) + (B^2 B_x^2 - B_y^2 B_z^2) \sin(2BT)), \\
[F_Q]_{\Sigma B_z \Sigma B_z} &= \frac{4}{B^4} (B_x^2 + B_y^2) (B_z^2 T^2 + \sin^2(BT)) \\
&\quad + \frac{\sin(2BT)}{B^6} (B_x^2 + B_y^2) (4BB_z^2 T + (B_x^2 + B_y^2) \sin(2BT)) \\
[F_Q]_{\Sigma B_x \Sigma B_y} &= \frac{4T}{B^4} (B_x B_y T (B_x^2 + B_y^2) + B_z \sin^2(BT) (B_x^2 - B_y^2)) \\
&\quad + \frac{\sin(2BT)}{B^6} (4BB_x B_y B_z^2 T - 2BB_z \sin^2(BT) (B_x^2 - B_y^2) - B_x B_y \sin(2BT) (B^2 + B_z^2)), \\
[F_Q]_{\Sigma B_x \Sigma B_z} &= \frac{4B_z}{B^4} (B_x T^2 (B_x^2 + B_y^2) - \sin^2(BT) (B_x + B_y B_z T)) \\
&\quad - \frac{\sin(2BT)}{B^6} (2BB_x B_z T (B^2 - 2B_z^2) + (B_x^2 + B_y^2) (2BB_y \sin^2(BT) - B_x B_z \sin(2BT))), \\
[F_Q]_{\Sigma B_y \Sigma B_z} &= \frac{4B_z}{B^4} (B_y T^2 (B_x^2 + B_y^2) - \sin^2(BT) (B_y - B_x B_z T)) \\
&\quad - \frac{\sin(2BT)}{B^6} (2BB_y B_z T (B^2 - 2B_z^2) - (B_x^2 + B_y^2) (2BB_x \sin^2(BT) + B_y B_z \sin(2BT))).
\end{aligned} \tag{S26}$$

Since the QFIM takes a block diagonal form, the estimation of the sum vector $\sum \vec{B}$ does not influence the precision of estimating the gradients $\nabla \vec{B}$, which can be expressed as:

$$(\delta \nabla B_{x_{\text{est}}})^2 + (\delta \nabla B_{y_{\text{est}}})^2 + (\delta \nabla B_{z_{\text{est}}})^2 \geq \text{Tr}(F_-^{-1}) = \frac{4B^2 - 3B_z^2}{16B^2 T^2} + \frac{5B^2 + 3B_z^2}{16 \sin^2(BT)}, \tag{S27}$$

where $B = \sqrt{B_x^2 + B_y^2 + B_z^2}$. We can verify that the weak commutativity condition in Eq.(S8) is satisfied, indicating the existence of a set of POVM that saturates the QCRB, achieving this precision.

For easier experimental realization, we consider performing local separable measurements on each sensor module (\mathcal{B} and \mathcal{C}). Specifically, one can choose the projective measurement in Bell basis on each sensor module as follows:

$$\Pi_{\mathcal{X}_{00}} = |\Phi^+\rangle\langle\Phi^+|, \quad \Pi_{\mathcal{X}_{01}} = |\Phi^-\rangle\langle\Phi^-|, \quad \Pi_{\mathcal{X}_{10}} = |\Psi^+\rangle\langle\Psi^+|, \quad \Pi_{\mathcal{X}_{11}} = |\Psi^-\rangle\langle\Psi^-|, \tag{S28}$$

where $\mathcal{X} \in \{\mathcal{B}, \mathcal{C}\}$ denoted the sensor module and the Bell states are given in Eq.(S16). This construction forms 16 measurement basis $\Pi_k = \Pi_{\mathcal{B}_i} \otimes \Pi_{\mathcal{C}_j}$, $\forall i, j \in \{00, 01, 10, 11\}$, satisfying $\sum_{k \in \{0000, \dots, 1111\}} \Pi_k = I$. The probability distribution of the measurement outcome under $\{\Pi_k\}$ gives $P_k = \langle \Psi_{\hat{x}} | \Pi_k | \Psi_{\hat{x}} \rangle$ for $k \in \{0000, 0001, \dots, 1111\}$, where $|\Psi_{\hat{x}}\rangle = U_S |\Psi_0\rangle$ is the evolved state. For certain measurement outcomes, such as $\{0011, 0111, 1011, 1100, 1101, 1110, 1111\}$, $P_k = 0$ regardless of the real values of $\nabla B_x, \nabla B_y, \nabla B_z$, indicating no information about the parameters can be obtained from these outcomes. In contrast, for $k \in \{0000, 0101, 1010\}$, $P_k = 0$ specifically at the zero-gradient, where $\nabla \vec{B} = (0, 0, 0)$. Even in this scenario, where the probability distribution equals zero at specific values, the probability distribution still contains implicit parameter information.

The classical Fisher information matrix (CFIM) depends on the derivative of P_k with respect to $x_i, x_j \in \{\nabla B_x, \nabla B_y, \nabla B_z, \sum B_x, \sum B_y, \sum B_z\}$, calculated as follows:

$$\begin{aligned}
[F_C]_{x_i x_j} &= \sum_k \frac{1}{P_k} \left(\frac{\partial P_k}{\partial x_i} \right) \left(\frac{\partial P_k}{\partial x_j} \right) \\
&= \sum_k \frac{(\partial x_i \langle \Psi_{\hat{x}} | \Pi_k | \Psi_{\hat{x}} \rangle) (\partial x_j \langle \Psi_{\hat{x}} | \Pi_k | \Psi_{\hat{x}} \rangle)}{\langle \Psi_{\hat{x}} | \Pi_k | \Psi_{\hat{x}} \rangle} \\
&= \sum_k \frac{4 \text{Re}(\langle \partial x_i \Psi_{\hat{x}} | \Pi_k | \Psi_{\hat{x}} \rangle) \text{Re}(\langle \partial x_j \Psi_{\hat{x}} | \Pi_k | \Psi_{\hat{x}} \rangle)}{\langle \Psi_{\hat{x}} | \Pi_k | \Psi_{\hat{x}} \rangle}
\end{aligned} \tag{S29}$$

where $k \in \{0000, 0001, 0010, 0100, 0101, 0110, 1000, 1001, 1010\}$. Specifically, at $\nabla B_x = 0, \nabla B_y = 0$ and $\nabla B_z = 0$, $P_k = \langle \Psi_{\hat{x}} | \Pi_k | \Psi_{\hat{x}} \rangle = 0$, $\text{Re}(\langle \partial x_i \Psi_{\hat{x}} | \Pi_k | \Psi_{\hat{x}} \rangle) = 0$ for $k \in \{0000, 0101, 1010\}$. In these cases, the term is of the form $\frac{0}{0}$ which needs to be calculated via limit. For these term, $[F_C]_{x_i x_j}$ can be calculated when the parameters $\nabla B_x, \nabla B_y$ and ∇B_z are displaced by an arbitrary small disturbance, replacing $|\Psi_{\hat{x}}\rangle$ with $|\Psi_{\hat{x}}\rangle + \sum_{l=1}^6 \delta x_l |\partial x_l \Psi_{\hat{x}}\rangle$, where $x_1 = \nabla B_x, x_2 = \nabla B_y, x_3 = \nabla B_z, x_4 = \sum B_x, x_5 = \sum B_y, x_6 = \sum B_z$. Thus, it can be verified that for $\forall x_i, x_j \in \{\nabla B_x, \nabla B_y, \nabla B_z, \sum B_x, \sum B_y, \sum B_z\}$,

$$\begin{aligned}
[F_C]_{x_i x_j} &= \sum_{k_1} \frac{\sum_{l_1=1}^6 \sum_{l_2=1}^6 4 \delta x_{l_1} \delta x_{l_2} \text{Re}(\langle \partial x_i \Psi_{\hat{x}} | \Pi_{k_1} | \partial x_{l_1} \Psi_{\hat{x}} \rangle) \text{Re}(\langle \partial x_{l_2} \Psi_{\hat{x}} | \Pi_{k_1} | \partial x_j \Psi_{\hat{x}} \rangle)}{\sum_{l_1=1}^6 \sum_{l_2=1}^6 \delta x_{l_1} \delta x_{l_2} \langle \partial x_{l_1} \Psi_{\hat{x}} | \Pi_{k_1} | \partial x_{l_2} \Psi_{\hat{x}} \rangle} \\
&\quad + \sum_{k_2} \frac{4 \text{Re}(\langle \partial x_i \Psi_{\hat{x}} | \Pi_{k_2} | \Psi_{\hat{x}} \rangle) \text{Re}(\langle \partial x_j \Psi_{\hat{x}} | \Pi_{k_2} | \Psi_{\hat{x}} \rangle)}{\langle \Psi_{\hat{x}} | \Pi_{k_2} | \Psi_{\hat{x}} \rangle} \\
&= [F_Q]_{x_i x_j}
\end{aligned} \tag{S30}$$

where $k_1 \in \{0000, 0101, 1010\}$ and $k_2 \in \{0001, 0010, 0100, 0110, 1000, 1001\}$. This demonstrates that the QCRB can be saturated by performing local projective measurement in the Bell basis on each sensor module, indicating the precision in Eq.(S27) is achievable.

Here, we also provide the precision achievable in estimating two components of gradients, specifically ∇B_x and ∇B_y , using the same non-local entangled probe state $|\Psi_0\rangle$. The quantum Fisher information matrix for simultaneously estimating $\nabla B_x, \nabla B_y, \sum B_x, \sum B_y$ also takes the block diagonal form in Eq.(S22), with F_- and F_+ given by

$$F_{\pm} = \begin{pmatrix} [F_Q]_{\nabla B_x \nabla B_x} & [F_Q]_{\nabla B_x \nabla B_y} \\ [F_Q]_{\nabla B_x \nabla B_y} & [F_Q]_{\nabla B_y \nabla B_y} \end{pmatrix}, \quad F_{\pm} = \begin{pmatrix} [F_Q]_{\sum B_x \sum B_x} & [F_Q]_{\sum B_x \sum B_y} \\ [F_Q]_{\sum B_x \sum B_y} & [F_Q]_{\sum B_y \sum B_y} \end{pmatrix}, \tag{S31}$$

where

$$\begin{aligned}
[F_Q]_{\nabla B_x \nabla B_x} &= \frac{4B_x^2 T^2}{B^2} + \frac{B_y^2 (16 \sin^2(BT) - 3 \sin^2(2BT))}{B^4}, \\
[F_Q]_{\nabla B_y \nabla B_y} &= \frac{4B_y^2 T^2}{B^2} + \frac{B_x^2 (16 \sin^2(BT) - 3 \sin^2(2BT))}{B^4}, \\
[F_Q]_{\nabla B_x \nabla B_y} &= \frac{4B_x B_y T^2}{B^2} - \frac{B_x B_y (16 \sin^2(BT) - 3 \sin^2(2BT))}{B^4}, \\
[F_Q]_{\Sigma B_x \Sigma B_x} &= \frac{4B_x^2 T^2}{B^2} + \frac{B_y^2 \sin^2(2BT)}{B^4}, \\
[F_Q]_{\Sigma B_y \Sigma B_y} &= \frac{4B_y^2 T^2}{B^2} + \frac{B_x^2 \sin^2(2BT)}{B^4}, \\
[F_Q]_{\Sigma B_x \Sigma B_y} &= \frac{4B_x B_y T^2}{B^2} - \frac{B_x B_y \sin^2(2BT)}{B^4},
\end{aligned} \tag{S32}$$

with $B = \sqrt{B_x^2 + B_y^2}$. The quantum Cramér-Rao bound can be saturated by performing projective measurement in Bell basis on each sensor module, where the proof of optimal measurement is similar to the three-component case and is omitted for brevity. Hence, the precision of estimating gradients is

$$\delta \nabla B_{x_{\text{est}}}^2 + \delta \nabla B_{y_{\text{est}}}^2 \geq \frac{1}{4T^2} + \frac{B^2}{4(1 + 3 \sin^2(BT)) \sin^2(BT)}. \tag{S33}$$

2. Local entanglement

To estimate the gradients between remote vector fields, a straightforward approach is to first estimate each vector field independently, then calculate the gradient. In this method, we use a 2-qubit locally entangled state to estimate the three components of each vector field. The unitary dynamics governing this system is represented by $U_s \otimes U_s$, where $U_s = e^{-iBT \mathbf{n} \cdot \boldsymbol{\sigma}}$. The analysis of precision limits follows [2]. The generator corresponding to the parameter $x_j \in \{B, \theta, \phi\}$ is

$$\begin{aligned}
G_{x_j} &= i (U_s^\dagger \otimes U_s^\dagger) (\partial_{x_j} U_s \otimes U_s + U_s \otimes \partial_{x_j} U_s) \\
&= h_{x_j} \otimes I_2 + I_2 \otimes h_{x_j}
\end{aligned} \tag{S34}$$

where h_{x_j} is given in Eq.(S9). By Eq.(S7), the diagonal elements of QFIM can be expressed as the variance of the generators G_{x_j} ,

$$[F_Q]_{x_j x_j} = 4 \langle \Delta^2 G_{x_j} \rangle = 4 \left(\langle G_{x_j}^2 \rangle - \langle G_{x_j} \rangle^2 \right), \tag{S35}$$

where the term $\langle G_{x_j}^2 \rangle$ and $\langle G_{x_j} \rangle^2$ can be expanded as

$$\begin{aligned}
\langle G_{x_j}^2 \rangle &= \langle h_{x_j}^2 \otimes I \rangle + \langle I \otimes h_{x_j}^2 \rangle + 2 \langle h_{x_j} \otimes h_{x_j} \rangle = 2c_{x_j}^2 + 2c_{x_j}^2 r_{x_j x_j}, \\
\langle G_{x_j} \rangle^2 &= c_{x_j}^2 (r_{x_j}^{(1)} + r_{x_j}^{(2)})^2.
\end{aligned} \tag{S36}$$

Here $r_{x_j x_j} = \text{Tr}[\rho_{SS}(\mathbf{n}_{x_j} \cdot \boldsymbol{\sigma}) \otimes (\mathbf{n}_{x_j} \cdot \boldsymbol{\sigma})]$, where ρ_{SS} is the density matrix for the probe state and \mathbf{n}_{x_j} are detailed in Eq.(S11). $r_{x_j}^{(1)} = \text{Tr}[\rho_S^{(1)} \mathbf{n}_{x_j} \cdot \boldsymbol{\sigma}]$ and $r_{x_j}^{(2)} = \text{Tr}[\rho_S^{(2)} \mathbf{n}_{x_j} \cdot \boldsymbol{\sigma}]$, where $\rho_S^{(1)}$ and $\rho_S^{(2)}$ are the reduced matrices of ρ_{SS} the first and second qubits.

For each parameter $x_j \in \{B, \theta, \phi\}$, we have $\delta x_{j\text{est}}^2 \geq \frac{1}{4\langle \Delta^2 G_{x_j} \rangle}$, thus

$$\begin{aligned}
& w_B \delta B_{\text{est}}^2 + w_\theta \delta \theta_{\text{est}}^2 + w_\phi \delta \phi_{\text{est}}^2 \\
& \geq \frac{1}{4} \left(\frac{w_B}{\langle \Delta^2 G_B \rangle} + \frac{w_\theta}{\langle \Delta^2 G_\theta \rangle} + \frac{w_\phi}{\langle \Delta^2 G_\phi \rangle} \right) \\
& = \frac{1}{4} \left(\frac{w_B/T^2}{2 + 2r_{BB} - (r_B^{(1)} + r_B^{(2)})^2} + \frac{w_\theta/\sin^2(BT)}{2 + 2r_{\theta\theta} - (r_\theta^{(1)} + r_\theta^{(2)})^2} + \frac{w_\phi/\sin^2(BT) \sin^2 \theta}{2 + 2r_{\phi\phi} - (r_\phi^{(1)} + r_\phi^{(2)})^2} \right) \\
& \geq \frac{1}{4} \left(\frac{w_B/T^2}{2 + 2r_{BB}} + \frac{w_\theta/\sin^2(BT)}{2 + 2r_{\theta\theta}} + \frac{w_\phi/\sin^2(BT) \sin^2 \theta}{2 + 2r_{\phi\phi}} \right) \\
& \stackrel{a)}{\geq} \frac{\left(\frac{\sqrt{w_B}}{T} + \frac{\sqrt{w_\theta}}{|\sin(BT)|} + \frac{\sqrt{w_\phi}}{|\sin(BT) \sin \theta|} \right)^2}{4(2 + 2r_{BB} + 2 + 2r_{\theta\theta} + 2 + 2r_{\phi\phi})} \\
& \stackrel{b)}{\geq} \frac{\left(\frac{\sqrt{w_B}}{T} + \frac{\sqrt{w_\theta}}{|\sin(BT)|} + \frac{\sqrt{w_\phi}}{|\sin(BT) \sin \theta|} \right)^2}{32}
\end{aligned} \tag{S37}$$

where the inequality *a)* follows from the Cauchy-Schwarz inequality, and the inequality *b)* uses the fact that $r_{BB} + r_{\theta\theta} + r_{\phi\phi} \leq 1$. To prove this fact, we write a general two-qubit state ρ as

$$\rho = \frac{1}{4} [I_4 + \sum_l r_l^{(1)} \sigma_l \otimes I + \sum_p r_p^{(2)} I \otimes \sigma_p + \sum_{l,p} r_{l,p} \sigma_l \otimes \sigma_p] \tag{S38}$$

where $l, p \in \{x, y, z\}$. Let $\rho_{SS} = (U_r \otimes U_r) \rho (U_r^\dagger \otimes U_r^\dagger)$, by using the properties in Eq.(S12), we have $r_{xx} = \text{Tr}[\rho(\sigma_x \otimes \sigma_x)] = \text{Tr}[\rho_{SS}(\mathbf{n}_\theta \cdot \boldsymbol{\sigma} \otimes \mathbf{n}_\theta \cdot \boldsymbol{\sigma})] = r_{\theta\theta}$, $r_{yy} = \text{Tr}[\rho(\sigma_y \otimes \sigma_y)] = \text{Tr}[\rho_{SS}(\mathbf{n}_\phi \cdot \boldsymbol{\sigma} \otimes \mathbf{n}_\phi \cdot \boldsymbol{\sigma})] = r_{\phi\phi}$ and $r_{zz} = \text{Tr}[\rho(\sigma_z \otimes \sigma_z)] = \text{Tr}[\rho_{SS}(\mathbf{n}_B \cdot \boldsymbol{\sigma} \otimes \mathbf{n}_B \cdot \boldsymbol{\sigma})] = r_{BB}$. Since the density matrix ρ is always positive semi-definite, let $r_l^{(1)} = 0$, $r_p^{(2)} = 0$ for $\forall l, p \in \{x, y, z\}$, and $r_{l,p} = 0$ for $l \neq p$, we have all the eigenvalues of ρ are non-negative, which gives the following constraints:

$$\begin{aligned}
r_{xx} + r_{yy} + r_{zz} & \leq 1 \\
r_{zz} - r_{xx} - r_{yy} & \leq 1 \\
r_{yy} - r_{xx} - r_{zz} & \leq 1 \\
r_{xx} - r_{yy} - r_{zz} & \leq 1
\end{aligned} \tag{S39}$$

The first inequality is equivalent to $r_{BB} + r_{\theta\theta} + r_{\phi\phi} \leq 1$. Hence, the lower bound on the figure of merit can be obtained as:

$$w_B \delta B_{\text{est}}^2 + w_\theta \delta \theta_{\text{est}}^2 + w_\phi \delta \phi_{\text{est}}^2 \geq \frac{\left(\frac{\sqrt{w_B}}{T} + \frac{\sqrt{w_\theta}}{|\sin(BT)|} + \frac{\sqrt{w_\phi}}{|\sin(BT) \sin \theta|} \right)^2}{32} \tag{S40}$$

which can be saturated when

$$\begin{aligned}
r_{BB}^{\text{opt}} & = \frac{3 \frac{\sqrt{w_B}}{T} - \frac{\sqrt{w_\theta}}{|\sin(BT)|} - \frac{\sqrt{w_\phi}}{|\sin(BT) \sin \theta|}}{\frac{\sqrt{w_B}}{T} + \frac{\sqrt{w_\theta}}{|\sin(BT)|} + \frac{\sqrt{w_\phi}}{|\sin(BT) \sin \theta|}} \\
r_{\theta\theta}^{\text{opt}} & = \frac{3 \frac{\sqrt{w_\theta}}{|\sin(BT)|} - \frac{\sqrt{w_B}}{T} - \frac{\sqrt{w_\phi}}{|\sin(BT) \sin \theta|}}{\frac{\sqrt{w_B}}{T} + \frac{\sqrt{w_\theta}}{|\sin(BT)|} + \frac{\sqrt{w_\phi}}{|\sin(BT) \sin \theta|}} \\
r_{\phi\phi}^{\text{opt}} & = \frac{3 \frac{\sqrt{w_\phi}}{|\sin(BT) \sin \theta|} - \frac{\sqrt{w_B}}{T} - \frac{\sqrt{w_\theta}}{|\sin(BT)|}}{\frac{\sqrt{w_B}}{T} + \frac{\sqrt{w_\theta}}{|\sin(BT)|} + \frac{\sqrt{w_\phi}}{|\sin(BT) \sin \theta|}}
\end{aligned} \tag{S41}$$

and $r_B^{(1)} + r_B^{(2)} = r_\theta^{(1)} + r_\theta^{(2)} = r_\phi^{(1)} + r_\phi^{(2)} = 0$. The lower bound can be saturated when the reduced two-qubit state takes the form:

$$\rho = \frac{1}{4}[I_4 + r_{BB}^{opt} \mathbf{n}_B \cdot \boldsymbol{\sigma} \otimes \mathbf{n}_B \cdot \boldsymbol{\sigma} + r_{\theta\theta}^{opt} \mathbf{n}_\theta \cdot \boldsymbol{\sigma} \otimes \mathbf{n}_\theta \cdot \boldsymbol{\sigma} + r_{\phi\phi}^{opt} \mathbf{n}_\phi \cdot \boldsymbol{\sigma} \otimes \mathbf{n}_\phi \cdot \boldsymbol{\sigma}], \quad (\text{S42})$$

indicating that this bound is unachievable without the introduction of an ancillary system. From the error propagation formula in Eq.(S20), we set $w_B = 1, w_\theta = B^2, w_\phi = B^2 \sin^2 \theta$, then the precision limits of estimating three components of a vector field is

$$\delta B_{x_{\text{est}}}^2 + \delta B_{y_{\text{est}}}^2 + \delta B_{z_{\text{est}}}^2 \geq \frac{1}{32} \left(\frac{1}{T} + \frac{2B}{|\sin(BT)|} \right)^2. \quad (\text{S43})$$

Without loss of generality, we set $\vec{B}_1 = \vec{B}_2 = \vec{B}$, the precision limit for estimating gradients $\nabla \vec{B} = \vec{B}_1 - \vec{B}_2 = (\nabla B_x, \nabla B_y, \nabla B_z)$ is

$$\delta \nabla B_{x_{\text{est}}}^2 + \delta \nabla B_{y_{\text{est}}}^2 + \delta \nabla B_{z_{\text{est}}}^2 \geq \frac{1}{16} \left(\frac{1}{T} + \frac{2B}{|\sin(BT)|} \right)^2. \quad (\text{S44})$$

It is important to note that achieving the ultimate precision as outlined in Eq.(S44) requires the use of an ancillary system, making this bound unattainable in practice. To ensure a fair comparison, we introduce a reference precision using maximally entangled states, represented by the probe state $|\psi\rangle = \frac{1}{\sqrt{2}}(|00\rangle + |11\rangle)$. The QFIM for estimating $\hat{x} = \{B, \theta, \phi\}$ by maximally entangled states is

$$F_Q = \begin{pmatrix} [F_Q]_{BB} & [F_Q]_{B\theta} & [F_Q]_{B\phi} \\ [F_Q]_{B\theta} & [F_Q]_{\theta\theta} & [F_Q]_{\theta\phi} \\ [F_Q]_{B\phi} & [F_Q]_{\theta\phi} & [F_Q]_{\phi\phi} \end{pmatrix} \quad (\text{S45})$$

with

$$\begin{aligned} [F_Q]_{BB} &= 4T^2 (3 + \cos(2\theta) + 2 \cos(2\phi) \sin^2 \theta), \\ [F_Q]_{\theta\theta} &= 2 \sin^2(BT) (3 + 3 \cos(2BT) \cos(2\phi) + 2 \sin^2 \phi + \cos^2(BT) (2 - 4 \cos(2\theta) \sin^2 \phi) \\ &\quad + 4 \cos \theta \sin(2BT) \sin(2\phi)), \\ [F_Q]_{\phi\phi} &= 2 \sin^2(BT) \sin^2 \theta (2 + 2 \sin^2(BT) + 2 \sin^2 \theta + 2 \sin^2 \phi + \cos(2BT) (\cos(2\theta) - 3 \cos(2\phi)) \\ &\quad + 2 \sin^2(BT) \cos(2\theta) \cos(2\phi) - 4 \sin(2BT) \cos \theta \sin(2\phi)), \\ [F_Q]_{B\theta} &= 4T (2 \sin^2(BT) \sin \theta \sin(2\phi) - \sin(2BT) \sin(2\theta) \sin^2 \phi), \\ [F_Q]_{B\phi} &= -16T \sin(BT) \sin^2 \theta \sin \phi (\cos(BT) \cos \phi + \sin(BT) \cos \theta \sin \phi), \\ [F_Q]_{\theta\phi} &= 2 \sin^2(BT) (\sin(2BT) \sin \theta ((3 + \cos 2\theta) \cos(2\phi) + 2 \sin^2 \theta) - 2 \cos(2BT) \sin(2\theta) \sin(2\phi)), \end{aligned} \quad (\text{S46})$$

which is a singular matrix. This means we cannot simultaneously estimate three components of the vector fields. Instead, we consider the optimal precision of estimating three parameters respectively, expressed as $\delta x_{j_{\text{est}}}^2 \geq \frac{1}{[F_Q]_{x_j x_j}}$ for $x_j \in \{B, \theta, \phi\}$, then we have the total precision for estimating three components of a vector field as

$$\begin{aligned} \delta B_{x_{\text{est}}}^2 + \delta B_{y_{\text{est}}}^2 + \delta B_{z_{\text{est}}}^2 &= \delta B_{\text{est}}^2 + B^2 \delta \theta_{\text{est}}^2 + B^2 \sin^2 \theta \delta \phi_{\text{est}}^2 \\ &\geq \frac{1}{[F_Q]_{BB}} + \frac{B^2}{[F_Q]_{\theta\theta}} + \frac{B^2 \sin^2 \theta}{[F_Q]_{\phi\phi}}. \end{aligned} \quad (\text{S47})$$

Thereby the corresponding precision for estimating the gradients is

$$\delta\nabla B_{x_{\text{est}}}^2 + \delta\nabla B_{y_{\text{est}}}^2 + \delta\nabla B_{z_{\text{est}}}^2 \geq \frac{2}{[F_Q]_{BB}} + \frac{2B^2}{[F_Q]_{\theta\theta}} + \frac{2B^2 \sin^2 \theta}{[F_Q]_{\phi\phi}}. \quad (\text{S48})$$

However, this precision is unachievable, which is a reference precision that equals the summation of the optimal precision for single-parameter estimation.

Now we turn the focus on estimating two components of gradients, $\hat{x} = (\nabla B_x, \nabla B_y)$. By a similar analysis as Eq.(S37), we have

$$\begin{aligned} w_B \delta B_{j_{\text{est}}}^2 + w_\phi \delta \phi_{j_{\text{est}}}^2 &\geq \frac{1}{4} \left(\frac{w_B}{\langle \Delta^2 G_B \rangle} + \frac{w_\phi}{\langle \Delta^2 G_\phi \rangle} \right) \\ &= \frac{1}{4} \left(\frac{w_B/T^2}{2 + 2r_{BB} - (r_B^{(1)} + r_B^{(2)})^2} + \frac{w_\phi/\sin^2(BT)}{2 + 2r_{\phi\phi} - (r_\phi^{(1)} + r_\phi^{(2)})^2} \right) \\ &\geq \frac{1}{4} \left(\frac{w_B/T^2}{2 + 2r_{BB}} + \frac{w_\phi/\sin^2(BT)}{2 + 2r_{\phi\phi}} \right) \\ &\stackrel{a)}{\geq} \frac{1}{4} \left(\frac{w_B}{4T^2} + \frac{w_\phi}{4\sin^2(BT)} \right) \end{aligned} \quad (\text{S49})$$

The inequality $a)$ is obtained by using the properties in Eq.(S39), which gives $r_{BB} \leq 1$ and $r_{\phi\phi} \leq 1$. Moreover, $r_{\theta\theta} \geq -1$ and by substitute $r_{BB} = r_{\phi\phi} = 1$ into constraints in Eq.(S39) gives the condition $r_{\theta\theta} \leq -1$. Hence, the inequality $b)$ is saturated when

$$r_{BB}^{\text{opt}} = 1, \quad r_{\theta\theta}^{\text{opt}} = -1, \quad r_{\phi\phi}^{\text{opt}} = 1, \quad (\text{S50})$$

and $r_B^{(1)} + r_B^{(2)} = r_\phi^{(1)} + r_\phi^{(2)} = 0$. The corresponding optimal probe state is

$$\rho = \frac{1}{4} [I_4 + \mathbf{n}_B \cdot \boldsymbol{\sigma} \otimes \mathbf{n}_B \cdot \boldsymbol{\sigma} - \mathbf{n}_\theta \cdot \boldsymbol{\sigma} \otimes \mathbf{n}_\theta \cdot \boldsymbol{\sigma} + \mathbf{n}_\phi \cdot \boldsymbol{\sigma} \otimes \mathbf{n}_\phi \cdot \boldsymbol{\sigma}] = |\psi_{\text{opt}}\rangle\langle\psi_{\text{opt}}| \quad (\text{S51})$$

Here $\theta = \frac{\pi}{2}$ and $|\psi_{\text{opt}}\rangle = \frac{1}{\sqrt{2}} (|+B\rangle^{\otimes 2} - |-B\rangle^{\otimes 2})$, where $|\pm B\rangle$ are the eigenstates of the generator h_B corresponding to the maximal and minimal eigenvalues respectively. With the optimal probe state, we can obtain the maximal QFIM for estimating $\hat{x} = \{B, \phi\}$ as

$$F_Q^{\text{max}} = \begin{pmatrix} 16T^2 & 0 \\ 0 & 16\sin^2(BT) \end{pmatrix} \quad (\text{S52})$$

Measurement in the Bell basis, as detailed in Eq.(S15), is the optimal measurement strategy that saturates the quantum Cramér-Rao bound. Hence, the bound in Eq.(S49) is achievable. By setting $w_B = 1$ and $w_\phi = B^2$, the corresponding precision of estimating two components of the vector field is

$$\delta B_{x_{\text{est}}}^2 + \delta B_{y_{\text{est}}}^2 = \delta B_{\text{est}}^2 + B^2 \delta \phi_{\text{est}}^2 \geq \frac{1}{16T^2} + \frac{B^2}{16\sin^2(BT)}, \quad (\text{S53})$$

thereby the ultimate precision for estimating the gradients under this strategy is

$$\delta\nabla B_{x_{\text{est}}}^2 + \delta\nabla B_{y_{\text{est}}}^2 \geq \frac{1}{8T^2} + \frac{B^2}{8\sin^2(BT)}. \quad (\text{S54})$$

It is worth mentioning that the optimal probe state in Eq.(S51) depends on the unknown parameters B and ϕ . However, the values of these parameters generally are not known as a priori. Instead, we must rely on estimated values, denoted as B_{est} and ϕ_{est} , which need to be adaptively updated in practice.

For easier experiment implementation, here, we also provide the precision of estimating gradient by using the maximally entangled state $|\psi\rangle = \frac{1}{\sqrt{2}}(|00\rangle + |11\rangle)$. The QFIM for estimating $\hat{x} = \{B, \phi\}$ by using maximally entangled state is

$$F_Q = \begin{pmatrix} 16T^2 \cos^2 \phi & -4T \sin(2BT) \sin(2\phi) \\ -4T \sin(2BT) \sin(2\phi) & 7 - 8 \cos(2BT) + 2 \cos(4BT) \cos^2 \phi - \cos(2\phi) \end{pmatrix} \quad (\text{S55})$$

The quantum Cramér-Rao bound can be saturated by using the projective measurement in Bell basis, as described in Eq.(S15). Hence, we have

$$\begin{aligned} \delta B_{\text{est}}^2 &= [\text{Cov}(\hat{x})]_{11} \geq [F_Q^{-1}]_{11} = \frac{1 - \cos^2(BT) \cos^2 \phi}{16T^2 \sin^2(BT) \cos^2 \phi}, \\ \delta \phi_{\text{est}}^2 &= [\text{Cov}(\hat{x})]_{22} \geq [F_Q^{-1}]_{22} = \frac{1}{16 \sin^4(BT)} \end{aligned} \quad (\text{S56})$$

Then the precision of estimating two components of the vector field by maximally entangled states is

$$\begin{aligned} \delta B_{x_{\text{est}}}^2 + \delta B_{y_{\text{est}}}^2 &= \delta B_{\text{est}}^2 + B^2 \delta \phi_{\text{est}}^2 \geq \frac{1}{16 \sin^2(BT)} \left(\frac{1 - \cos^2(BT) \cos^2 \phi}{T^2 \cos^2 \phi} + \frac{B^2}{\sin^2(BT)} \right) \\ &= \frac{1}{16 \sin^2(BT)} \left(\frac{B^2 - \cos^2(BT) B_x^2}{T^2 B_x^2} + \frac{B^2}{\sin^2(BT)} \right). \end{aligned} \quad (\text{S57})$$

Similarly, the precision for estimating the gradients by maximally entangled states is

$$\delta \nabla B_{x_{\text{est}}}^2 + \delta \nabla B_{y_{\text{est}}}^2 \geq \frac{1}{8 \sin^2(BT)} \left(\frac{B^2 - \cos^2(BT) B_x^2}{T^2 B_x^2} + \frac{B^2}{\sin^2(BT)} \right). \quad (\text{S58})$$

3. Strategy comparison

In addition to the two gradient-sensing approaches discussed above—direct gradient estimation using non-local entanglement (NLE) and a two-step approach that first estimates each vector field with local entanglement (LE) separately before calculating the gradient—we also consider an alternative approach based on the remote sensing (RS) described in the first section. In this approach, the remote magnetic fields at each location are estimated independently, with the central module serving as an ancilla, and the gradient is calculated from the separate field estimates. For a more comprehensive comparison, we also present the precision of gradient estimation achievable with this alternative strategy. The comparison is made under the condition that the resource allocation is identical, with each sensor module containing two sensors. In the following tables, we list the precision achieved by various strategies for estimating gradients in two and three directions, respectively.

In the main text, we have provided a detailed theoretical and experimental comparison of various strategies for estimating a two-component gradient. For completeness, Figure S1 gives the

Strategy	Initial state	Precision	Optimality	Achievability
NLE	$\frac{1}{\sqrt{2}} (0011\rangle - 1100\rangle)$	$\frac{4B^2-3B_z^2}{16B^2T^2} + \frac{5B^2+3B_z^2}{16\sin^2(BT)}$	N	Y
RS	$\frac{1}{\sqrt{2}} (00\rangle + 11\rangle)$	$\frac{1}{4T^2} + \frac{B^2}{2\sin^2(BT)}$	Y	Y
LE	N.A.	$\frac{1}{16} \left(\frac{1}{T} + \frac{2B}{ \sin(BT) } \right)^2$	Y	N
	$\frac{1}{\sqrt{2}} (00\rangle + 11\rangle)$	$\frac{2}{[F_Q]_{BB}} + \frac{2B^2}{[F_Q]_{\theta\theta}} + \frac{2B^2 \sin^2 \theta}{[F_Q]_{\phi\phi}}$	N	N

Table S1. The precision for estimating gradients along x, y and z directions.

Strategy	Initial state	Precision	Optimality	Achievability
NLE	$\frac{1}{\sqrt{2}} (0011\rangle - 1100\rangle)$	$\frac{1}{4T^2} + \frac{B^2}{4(1+3\sin^2(BT))\sin^2(BT)}$	N	Y
RS	$\frac{1}{\sqrt{2}} (00\rangle + 11\rangle)$	$\frac{1}{4T^2} + \frac{B^2}{4\sin^2(BT)}$	Y	Y
LE	$\frac{1}{\sqrt{2}} (+B\rangle^{\otimes 2} - -B\rangle^{\otimes 2})$	$\frac{1}{8T^2} + \frac{B^2}{8\sin^2(BT)}$	Y	Y
	$\frac{1}{\sqrt{2}} (00\rangle + 11\rangle)$	$\frac{1}{8\sin^2(BT)} \left(\frac{B^2 - \cos^2(BT)B_z^2}{T^2B_z^2} + \frac{B^2}{\sin^2(BT)} \right)$	N	Y

Table S2. The precision for estimating gradients along x and y directions.

comparison of strategies for estimating a three-component gradient. To ensure a fair comparison, we include the precision limit of Strategy LE utilizing maximally entangled states. Although employing the theoretically unachievable lower bound of Strategy LE, as derived in Eq.(S44), may not seem fair, it still highlights the enhanced precision of Strategy NLE across certain parameter value ranges. For example, at $B = 1$ and $\theta = \pi/2$, Strategy NLE demonstrates higher precision than Strategy LE during short encoding times T . Notably, despite the initial state of Strategy NLE not being optimal, and hence not achieving the highest possible precision, it still surpasses the best precision achievable by strategies without non-local entanglement. This emphasizes the significant advantages of distributed quantum sensing, demonstrating its superiority in achieving enhanced precision.

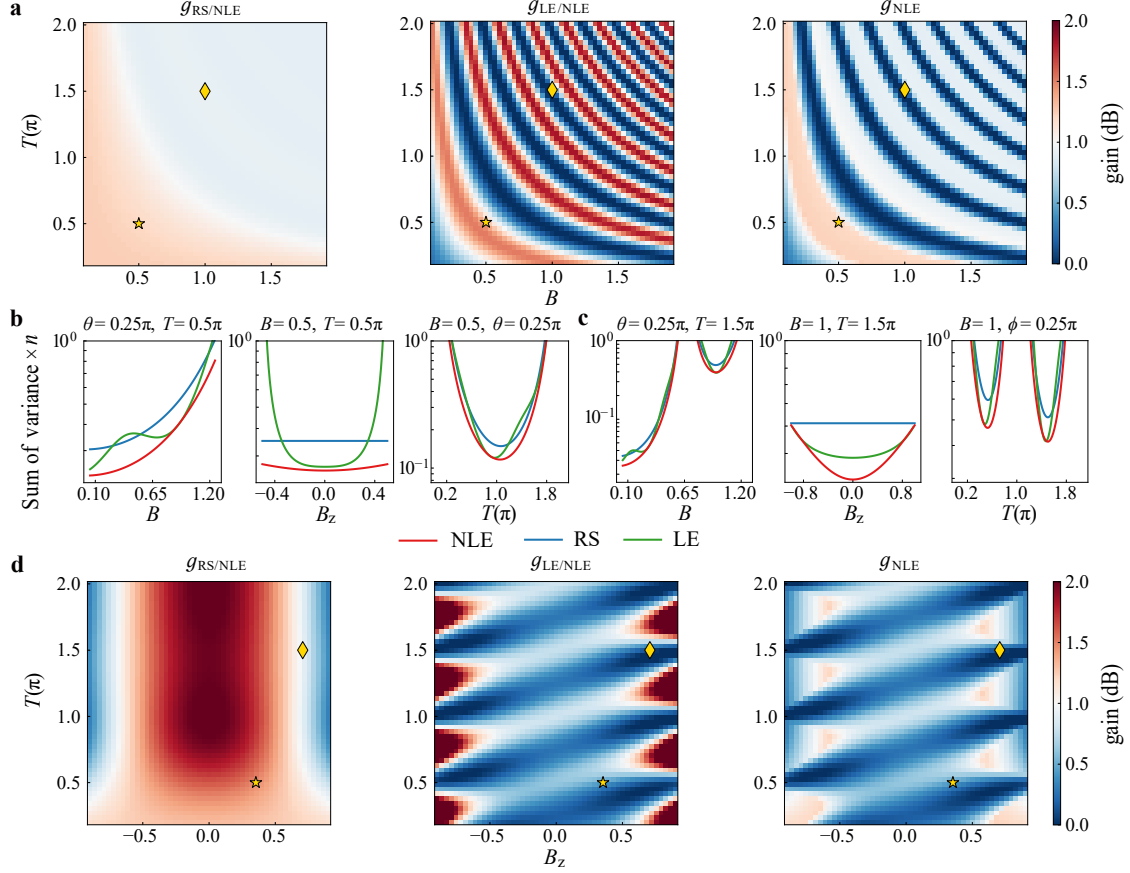


Fig. S1. **Comparing different strategies for estimating a 3-component gradient.** The x -component and y -component of the gradient are set of equivalent proportions. The stars mark the parameter set: $B = 0.5, T = 0.5\pi$; the diamonds mark the parameter set: $B = 1, T = 1.5\pi$. **a**, The advantage of NLE at $\theta = \pi/4$ when B and T are varying. **b**, The precision limits of three strategies around $B = 0.5, T = 0.5\pi$. Left: θ and T are fixed, B is varying from 0.05 to 1.25. Middle: B and T are fixed, B_z is varying from -0.5 to 0.5 . Right: B and θ are fixed, T is varying from 0.1π to 1.9π . **c**, The precision limits of three strategies around $B = 1, T = 1.5\pi$. Left: θ and T are fixed, B is varying from 0.05 to 1.25. Middle: B and T are fixed, B_z is varying from -0.9 to 0.9 . Right: B and θ are fixed, T is varying from 0.1π to 1.9π . **d**, The advantage of NLE at $B = 1$ when B_z and T are varying. In **a** and **d**, the left panels exhibit the gain of NLE over RS; the middle panels exhibit the gain of NLE over LE; the right panels exhibit the product of the gain of NLE over RS and the gain of NLE over LE.

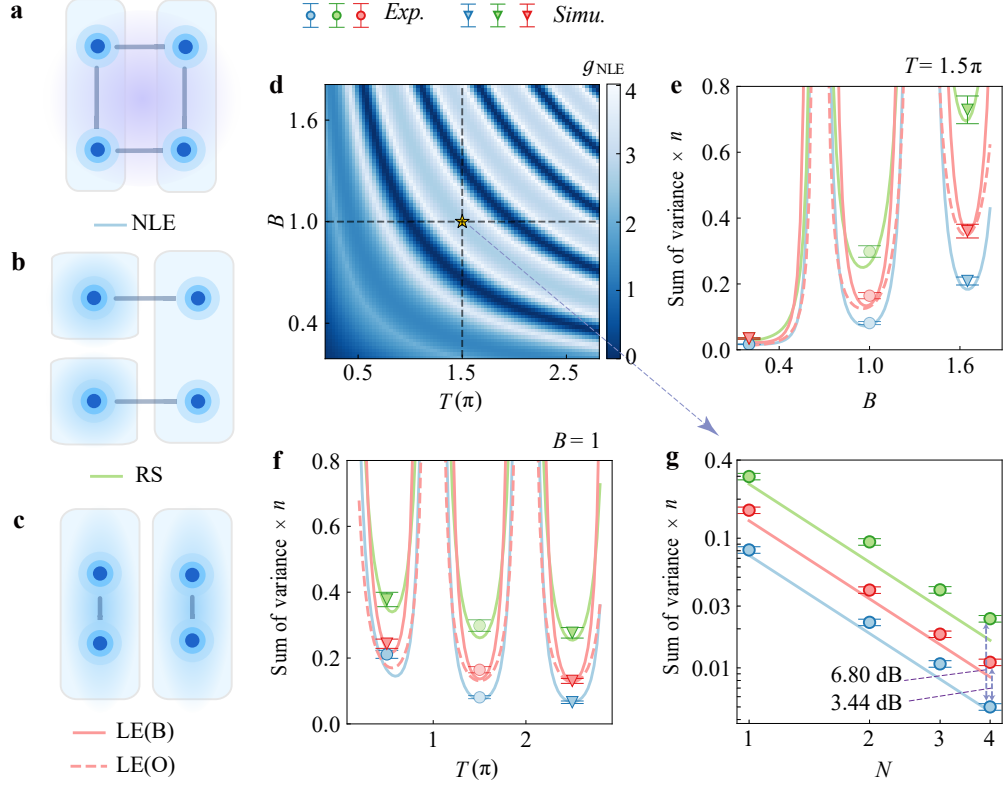


Fig. S2. **Strategies comparison for gradient estimation of a 2-component vector field.** **a-c**, Schematic diagrams of different strategies: **(a)** Distributed sensing with non-local entanglement (NLE); **(b)** Remote sensing (RS) with an ancilla qubit; **(c)** Sensing with local entanglement (LE). **d**, Parameter range where NLE outperforms RS and LE. The minimum precision gain of NLE over RS and LE(B) across different B and T values, is calculated by their theoretical precision. **e-f**, Comparison of the precision ($\sum_{i \in \{x,y\}} \delta^2 \nabla B_{i_{\text{est}}}$) of the three strategies. **(e)** Precision versus B for the three strategies at $T = 1.5\pi$ and $N = 1$. **(f)** Impact of T on estimation precision at $B = 1$ and $N = 1$. **(g)** Estimation precision versus N for the three strategies at $T = 1.5\pi$ and $B = 1$. The solid and dashed curves: the theoretical precision bound. LE(B): local entanglement strategy using Bell state as the probe state, and Bell measurement. LE(O): local entanglement strategy using the optimal probe state and measurement.

II. EXPERIMENTAL IMPLEMENTATION

A. Device information

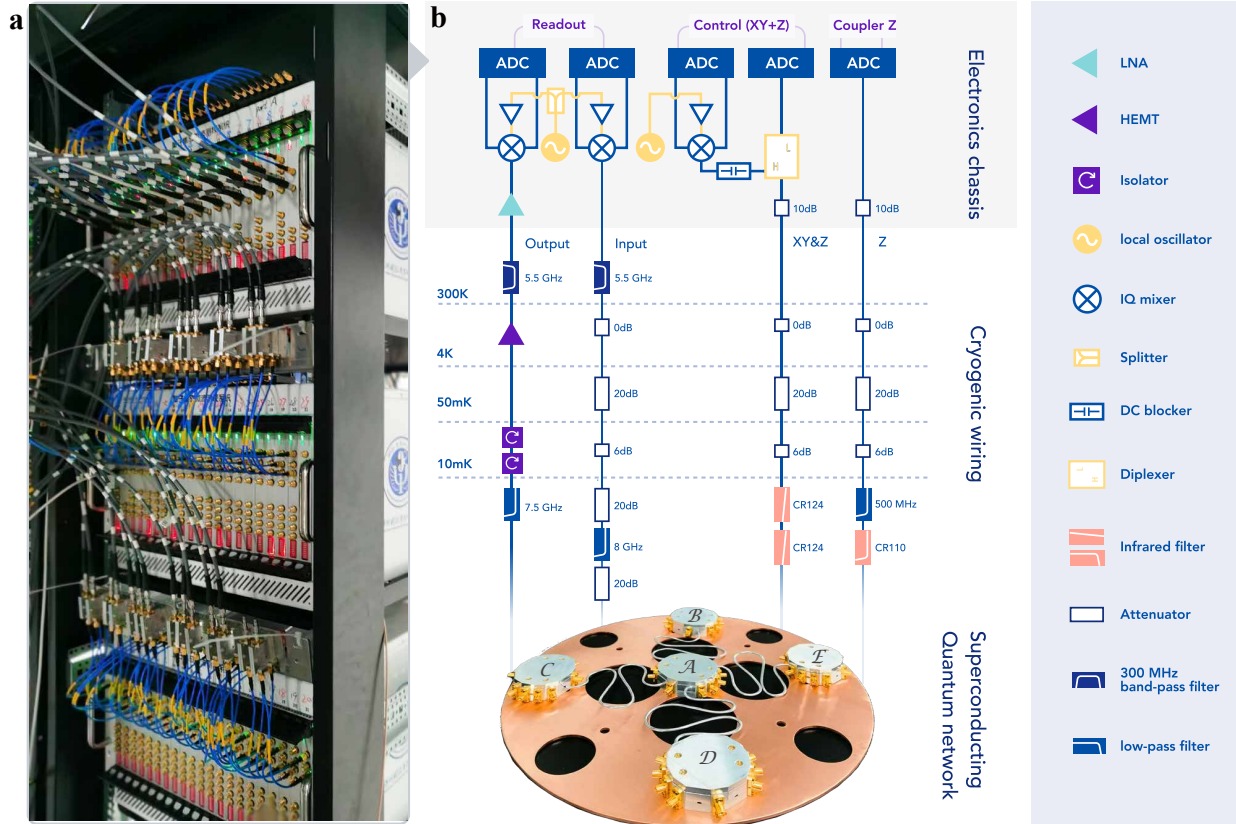


Fig. S3. **The experimental setup.** **a**, The microwave control and measurement system built for this experiment. **b**, The schematic diagram of the room-temperature electronics chassis, cryogenic wiring and superconducting quantum network inside of the dilution refrigerator. Right panel: the legend of the devices.

We implement the distributed quantum metrology experiment utilizing a modular quantum computing platform composed of five superconducting quantum chips, each integrated with four qubits. The inter-chip connectivity is facilitated by high-quality aluminum superconducting coaxial cables, where a gmon coupler is positioned between the qubits engaged in communication and the cable, enabling tunable coupling strength. Furthermore, an impedance transformer is designed on chip to significantly mitigate the stray loss on the communication channels [3]. In Fig. S3, we show the comprehensive structure of the experimental setup. The distributed quantum processors are sheltered in the 10 mK environment, nestled beneath the mixing chamber of a dilution refrigerator. The microwave cables connecting the superconducting quantum chips serve as the conduit for signal transmission and reception between the quantum processors (see the bottom part of the middle panel) and the customized integrated electronic channels (see the left photograph). The electron-

ics is primarily composed of digital-to-analog converters (DAC) and analog-to-digital converters (ADC), which orchestrate the generation, manipulation and readout of quantum control signals. The generation of XY control signals (single-qubit rotation) is facilitated by IQ mixing of the MHz output of the DACs and the GHz microwave carrier from a local oscillator (LO). Concurrently, the Z control signals (qubit frequency modulation) originate from DC and pulse signals output of the DACs. The XY signals and Z signals belonging to each qubit are combined with a customized diplexer in room temperature. The readout pulses are generated by another set of DACs, LO and IQ mixers, these devices up-convert the probe photons to match the readout resonator frequencies, conversely, the emitted photonic signals from the readout resonators are amplified and down-converted, finally being sampled by the ADCs, completing the readout cycle and providing a digital record of the measurement data. For higher control and readout quality, we deploy multiple filters across different temperature zones within the experimental setup (see the middle panel), the legends detailing the components of these stages are shown in the adjacent panel on the right.

Node	A		B		C	
Qubit	Q_1	Q_2	Q_3	Q_4	Q_5	Q_6
$\omega_{\text{idle}}/2\pi$ (GHz)	4.551	5.019	4.477	4.959	4.937	4.393
$\omega_{\text{read}}/2\pi$ (GHz)	5.629	5.692	5.686	5.627	5.688	5.621
$E_C/2\pi$ (MHz)	-212	-200	-210	-225	-210	-229
F_{00}	0.94	0.94	0.88	0.86	0.92	0.90
F_{11}	0.91	0.90	0.87	0.83	0.88	0.89
T_1 (μs)	19.2	18.4	26.8	14.3	25.3	26.2
T_{2R} (μs)	1.52	4.77	2.42	4.72	3.58	4.02
T_{2E} (μs)	5.49	10.95	11.49	15.18	15.57	14.45
SQG RB fid (%)	99.96	99.91	99.95	99.47	99.80	99.75
CZ XEB fid (%)	98.50		97.30		98.40	

Table S3. Device information

The experiment in this work involves three distributed quantum processors, each containing two qubits. We list the basic information of these six qubits in Table S3. All qubits are designed to be operated across a frequency range of 4.1 \sim 5.1 GHz, and idled at staggered frequencies. The resonator frequencies are also staggered for independent readout. The anharmonicity E_C is a parameter determined by the capacitance of each qubit, it is instrumental in shaping the interaction essential for the construction of CZ gates. F_{00} and F_{11} are the state preparation and measurement (SPAM) fidelity for $|0\rangle$ and $|1\rangle$. T_1 parameter denotes the energy relaxation time of each qubit, T_{2R} and T_{2E} represent the dephasing time characterized by Ramsey experiment and spin echo experiment, respectively.

B. Gate performance

We calibrate the CZ gates with a standard protocol[4]. We obtain CZ gate pulse with 36 ns plateau and 10 ns flattop rising and falling edges, and this gate is benchmarked using cross-entropy benchmarking (XEB) experiment [5], the fidelity turns out to be 98.1% in average.

The state transfer operation is calibrated by vacuum Rabi experiments between the inter-chip cable and the communication qubit to synchronize the frequencies of two qubits connecting on either side of the cable, aligning them to resonance. Concurrently, we tune the pulses applied on the tunable couplers to achieve an optimal coupling strength, reaching a low reflection loss[3]. The averaged transferred state fidelity measured by quantum state tomography is $\sim 98.4\%$.

The control-signal sequence is implemented by gate sets in $U(3)$ formalism: $U_3(\alpha, \beta, \lambda) = R_z(\beta)R_x(\pi/2)R_z(\alpha)R_x(-\pi/2)R_z(\lambda)$. The gate set consists of three Z gates with three independent angles (λ, α, β) . These Z gates are interleaved with an $X/2$ gate and a $-X/2$ gate. The single qubit gates (SQG) are benchmarked by randomized benchmarking (RB) experiment, and we obtain an averaged fidelity: 99.81%.

C. Implementation of distributed sensing in quantum circuits

The NLE strategy for gradient metrology is realized as illustrated in Fig. S4. We construct a three-node sensor network comprising modules \mathcal{A} , \mathcal{B} , \mathcal{C} . Initially, We generate a Bell pair between Q_1 and Q_2 on module \mathcal{A} , then simultaneously transfer one qubit of this pair from Q_1 to Q_3 on module \mathcal{B} and another from Q_2 to Q_5 on module \mathcal{C} . Immediately thereafter, we apply CNOT gates on both \mathcal{B} and \mathcal{C} , and obtain the GHZ state across module \mathcal{B} and \mathcal{C} , with a fidelity of 80.36% (see Fig. S4(c)). The probe state $|\Psi_0\rangle$ is prepared by applying additional X gates on Q_3 and Q_4 , and a Z gate on Q_5 , achieving a fidelity of 76.16% (see Fig. S4(d)). Subsequently, we encode the spatially distributed vector field on sensor chips \mathcal{B} and \mathcal{C} with $U(3)$ -formalism gate sets, where \vec{B}_1 is acting on both Q_3 and Q_4 , \vec{B}_2 is acting on both Q_5 and Q_6 . Following the encoding process, we conduct Bell measurement on both modules \mathcal{B} and \mathcal{C} . Under optimal control, the ideal final state $|\Psi_f\rangle$ has equivalent occupation on $|0010\rangle$ and $|1000\rangle$, the fidelity obtained from experiment is 75.20% (see Fig. S4(e)). The information carried on the sensors are decoded into the probability distribution in measurement basis (see Fig. S4(f) for P_{0010}). The oscillation period over gradient components ∇B_x and ∇B_y are observed to reduce with increasing sequential copies N .

The error in this sequence primarily stems from the control error when synchronously transferring two entangling states. The control error is estimated to be 11.44% for generating the non-local GHZ state, the decoherence error throughout this 340 ns sequence is approximately 8.34%, estimated by numerical simulation. These two parts yields an estimated fidelity of 80.22%, which is closed to our experimental result of 80.36%. The non-local entangling state across two chips, which are not directly connected, is more fragile to environmental noise. The effective decoherence

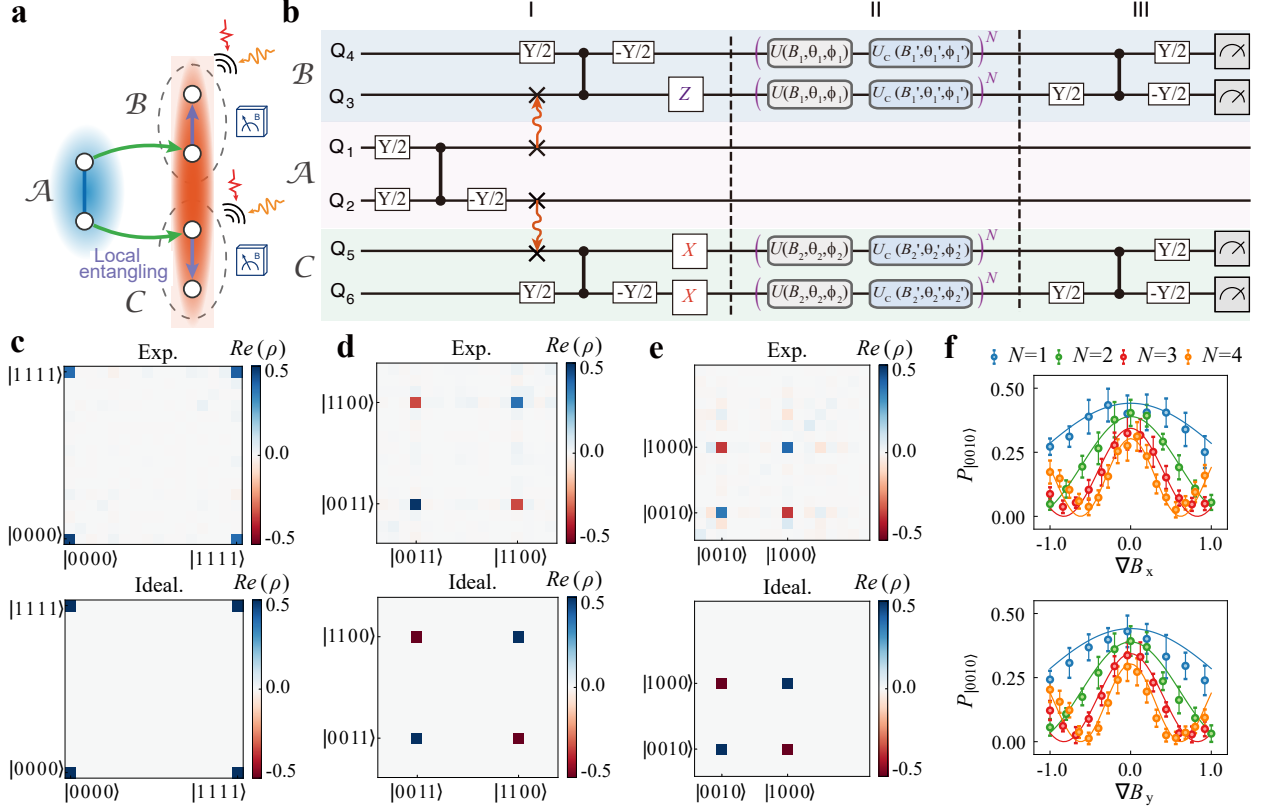


Fig. S4. **a**, A brief schematic diagram of NLE metrology strategy for gradient. **b**, The detailed quantum circuit of (a). **c**, The remote four-qubit GHZ state generated across three modules. **d**, The four-qubit probe state $|\Psi_0\rangle = \frac{1}{\sqrt{2}}(|0011\rangle - |1100\rangle)$. **e**, The reference final state $|\Psi_f\rangle = \frac{1}{\sqrt{2}}(|0010\rangle - |1000\rangle)$ after step III, with no control and signal units inserted into the circuit. **f**, The probability oscillation observed when scanning parameter ∇B_x or ∇B_y for different N , the encoding time is fixed at $T = 0.2\pi$.

rate of the probe state is estimated to be $80 \times 2\pi$ kHz by numerical analysis. As a consequence, the fidelity values of $|\Psi_f\rangle$ are 69.27%, 63.81%, 58.78%, 54.15% for $N = 1 \sim 4$, respectively. These values are higher than the confidence threshold $\sim 50\%$ for entanglement.

Demonstrating RS strategy requires two pairs of distributed nodes ($\mathcal{A}-\mathcal{B}$ and $\mathcal{A}-\mathcal{C}$) with high-quality connection. We take $\mathcal{A}-\mathcal{B}$ as an example (Fig. S5a), we transfer the local entanglement (indicated by the blue shadow) to a remote node, thereby establishing the cross-module entanglement (indicated by the red shadow). In our conception, the metrology of a local field through a sensor network comprising a central measurement module and multiple sensor modules spatially positioned for sensing. The quantum circuit is illustrated in Fig. S5(b). Initially, we generate a local Bell state on chip \mathcal{A} , and subsequently transfer this entangled state from Q_2 on chip \mathcal{A} to Q_3 on module \mathcal{B} , resulting in a cross-node Bell state between Q_1 and Q_3 . Immediately following the probe state preparation, we use Q_3 as the sensor qubit, Q_1 as the ancillary qubit. Assisted with dynamical decoupling sequence on Q_1 and Q_2 , the inter-module entanglement is preserved from fast decoherence, until the quantum state on Q_3 is retrieved back to Q_2 . The last step of this

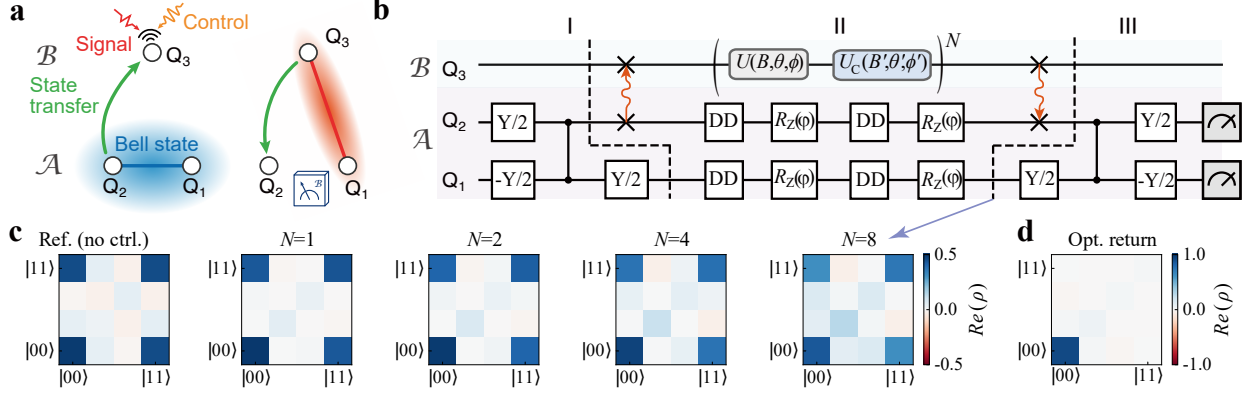


Fig. S5. **a**, A brief schematic diagram for sensing a local vector field at a certain position with two nodes \mathcal{A} and \mathcal{B} . **b**, The quantum circuit diagram for **a**: I: state preparation, II: encoding, III: measurement. **c**, Ref (no ctrl): the density matrix with no signal-control sequence, measured after step II. $N = 1 \sim 4$: the density matrices with $N = 1, 2, 4, 8$, measured after step II. **d**, Opt return: the density matrix with no signal-control sequence, measured after step III.

process involves applying a Bell measurement on Q_1, Q_2 . Under the optimal control conditions, step II behaves as an identity operator. We proceed to conduct quantum state tomography on module \mathcal{A} after the encoded quantum state is retrieved. Fig. S5(c) shows the extracted real part of density matrices from Q_2 and Q_3 .

The reference circuit, devoid of control and signal encoding in step II, achieves a final state fidelity of 91.15%. For $N = 1, 2, 4, 8$ in step II, we attain state fidelities of 88.13%, 84.37%, 79.02%, 70.46%, respectively. The reference final state is presented in the rightmost panel, the state fidelity is 90.52%. In this sequence, control error from the CNOT gates and state transfer operations amounts to 8.7%, the control error from each U_x or U_c unit is 0.79% in average, while the average decoherence error per unit is 2.55%, stemming from an effective decoherence rate of $41.1 \times 2\pi$ KHz.

A straightforward feature of the relation between control-signal layer N and the estimated precision can be captured by the oscillation period of probability under Bell measurement. As is shown in Fig. S6, the period of P_{00} profile near the optimal control parameters decreases at a rate proportional to N . Scanning each single parameter is analogous to a single-parameter-estimation process, wherein the quantum Fisher information is determined by the derivative of probability with respect to the parameter to be estimated. Therefore, this allows us to have an intuitive perception of the enhancement from sequential strategy. Moreover, the encoding time T is also periodically correlated to the probability distribution, and this correlation depends on the signal parameters. For example, when the signal is set to $(B, \theta, \phi) = (1, \pi/4, \pi/4)$, the period of P_{00} profile at $T = \pi, 2\pi$ stays invariant with respect to the parameters θ and ϕ , regardless of N . In contrast, at $T = 0.5\pi$ or $T = 1.5\pi$, the oscillation period changes more dramatically, indicating that the sequential strategy is effective there.

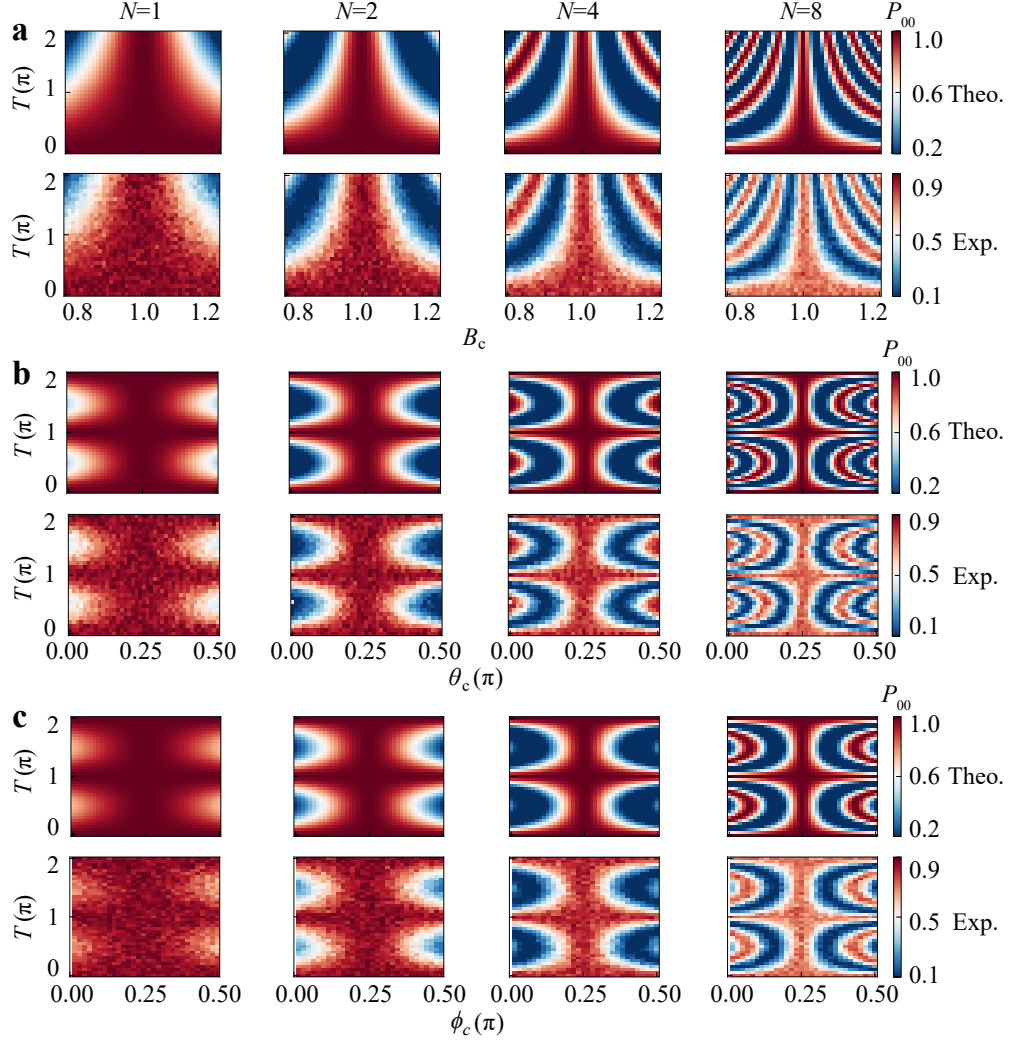


Fig. S6. **The probability oscillation with three parameters and encoding time T .** **a**, For a fixed signal, we scan control parameter B_c and encoding time T for different N . **b**, We scan control parameter θ_c and encoding time T for different N . **c**, We scan control parameter ϕ_c and encoding time T for different N .

To implement LE strategy, we generate local Bell state on node \mathcal{B} and \mathcal{C} , signals and controls are simultaneously acting on two pairs of sensor qubits. The sequence ends with Bell measurement on \mathcal{B} and \mathcal{C} , which is similar to RS strategy.

III. EXTENDED DATA

A. Extended data for sensing of remote vector fields

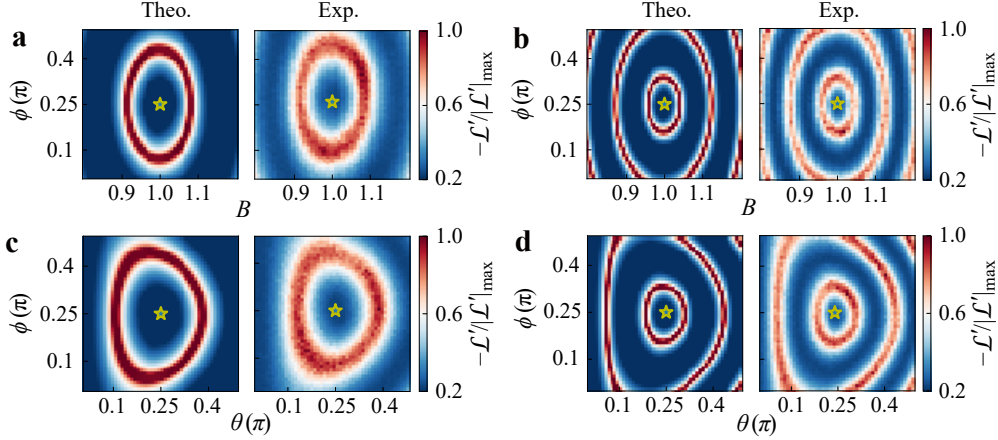


Fig. S7. **The likelihood function landscape at $N = 4$ and $N = 8$.** Stars: the location of the optimal control parameters. **a**, The landscape for parameter B and ϕ at $N = 4$. **b**, The landscape for parameter B and ϕ at $N = 8$. **c**, The landscape for parameter θ and ϕ at $N = 4$. **d**, The landscape for parameter θ and ϕ at $N = 8$. We post the theoretical landscape and experimental result, and mark the optimal control parameters.

We benchmark the sensor-ancilla network by analyzing the landscape of the likelihood function \mathcal{L}' near the optimal control parameters, the results are shown over two variables in Fig. S7. Specifically, the panels depict $\mathcal{L}'(B, \phi)$ in Fig. S7a,b and $\mathcal{L}'(\theta, \phi)$ in Fig. S7c,d. The optimal control parameters, marked with a star in each panel, correspond to the expected estimation results. As N increases, the boundary area of the likelihood landscape contracts, demonstrated for $N = 4$ in Fig. S7a,c and $N = 8$ in Fig. S7b,d. The agreement between theoretical and experimental results ensures that the estimated parameters not only align with the observed data but also adhere to the underlying physical model.

The Fig. S8 illustrates the complete MLE result for sensing the three-component vector field. The density amplitude in each panel represents the count of distribution normalized by the integral of distribution at $N = 1$. These results demonstrate that increasing the number of sequential copies enhances the precision of simultaneous three-parameter estimation. However, unavoidable experimental errors introduce a bias of up to $\pm 3.45\%$ in the averaged estimation results, deviating from the actual vector field parameters. These errors can distort the likelihood landscape, affecting the efficiency of the MLE process. Moreover, fluctuation in experimental noise lead to inhomogeneous probability distributions, increasing the risk of convergence to local rather than global minima. Despite these challenges, the optimal strategy we implement facilitates a flat region around the optimal control parameters, and the use of multiple initial values mitigates the impact of local minima [6]. This approach improves the robustness and reliability of the estimation process [7].

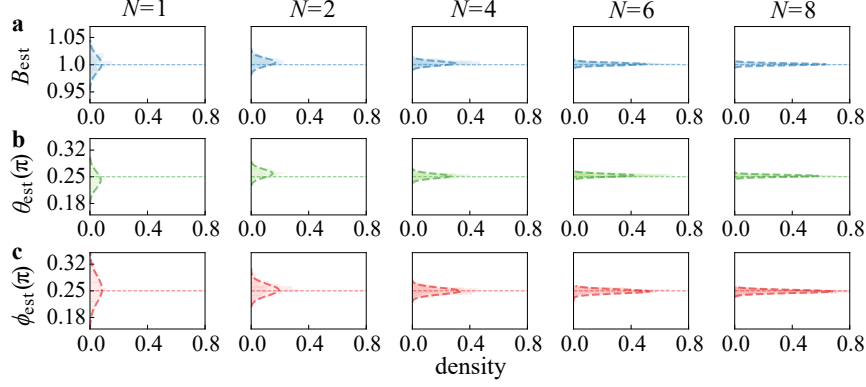


Fig. S8. **The result for simultaneously estimating three parameters of a local vector field $\vec{B}(B, \theta, \phi)$.** Bars: MLE result histograms. Dashed curves: gaussian fitting of the histograms. Dashed lines: the ideal signal parameters. **a**, The density distribution of parameter B . **b**, The density distribution of parameter θ . **c**, The density distribution of parameter ϕ .

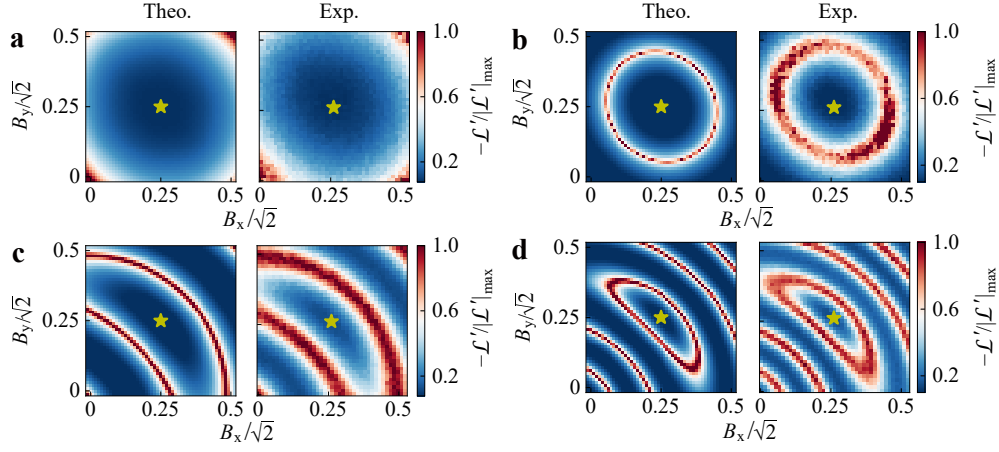


Fig. S9. **The theoretical and experimental landscape of estimating a two-component vector field with a sensor-ancilla network.** Stars: the location of the optimal control parameters. **a**, At $N = 2$ and $T = 0.5\pi$. **b**, At $N = 4$ and $T = 0.5\pi$. **c**, At $N = 2$ and $T = 1.5\pi$. **d**, At $N = 4$ and $T = 1.5\pi$

We apply the same benchmarking approach to a two-component vector field. As is shown in Fig. S9, the contraction of the likelihood function landscape with increasing N is evident. The parameters to be estimated in this case are set as $\vec{B} = (\frac{\sqrt{2}}{2}, \frac{\sqrt{2}}{2}, 0)$, corresponding to $|\vec{B}| = 0.5$.

B. Extended data for distributed sensing of vector field gradient

We experimentally evaluate the performance of NLE strategy for simultaneously estimating the three components of the gradient. In this scheme, we set $\vec{B} = (\frac{1}{2}, \frac{1}{2}, \frac{\sqrt{2}}{2})$, the normalized distributions of the estimators $\nabla B_{x_{\text{est}}}$, $\nabla B_{y_{\text{est}}}$, and $\nabla B_{z_{\text{est}}}$ are shown in Fig. S10a (for $T = 0.5\pi$) and Fig. S10b (for $T = 1.5\pi$).

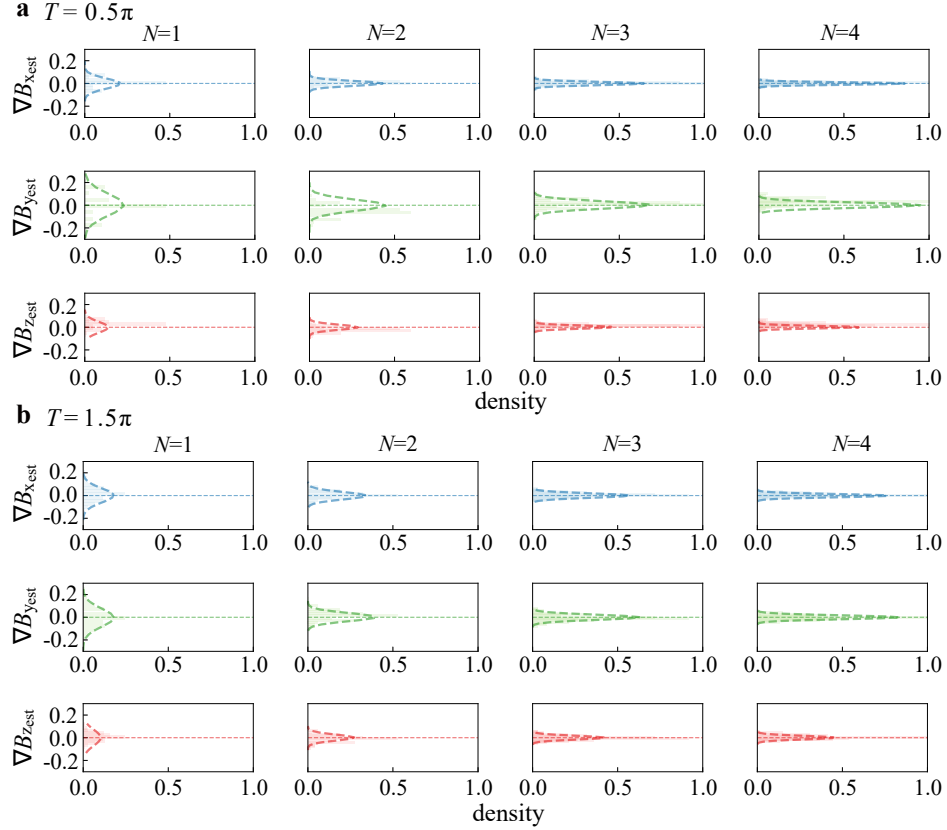


Fig. S10. **The normalized distribution of estimators for simultaneously three-component estimation.** Bars: MLE result histograms. Dashed curves: gaussian fitting of the histograms. Dashed lines: the ideal signal parameters. **a**, At $T = 0.5\pi$ and $N = 1 \sim 4$. **b**, At $T = 1.5\pi$ and $N = 1 \sim 4$.

When estimating the gradient of a two-component vector field $\nabla\vec{B} = (\nabla B_x, \nabla B_y)$, the field amplitudes are expressed as a function of gradient $\nabla\vec{B}$ and sum $\sum\vec{B}$ at two distinct positions, with $\vec{B}_1 = (\sum\vec{B} + \nabla\vec{B})/2$ and $\vec{B}_2 = (\sum\vec{B} - \nabla\vec{B})/2$. The full dataset, presented in Fig. 2 of the main text, is shown in Fig. S11, where the x and y components are plotted separately. The signal parameters are chosen as $\sum\vec{B} = (\sqrt{2}/2, \sqrt{2}/2, 0)$ and $\nabla\vec{B} = (0, 0, 0)$. The encoding times are set to $T = 0.5\pi$ (Fig. S11a) and $T = 1.5\pi$ (Fig. S11b).

C. The influence of noise

Different types of noise in quantum system have impact to the precision of the gradiometer. The effects of noisy channels in quantum parameter estimation have been discussed in previous studies [8–13]. In our work, the dominant sources of noise are control errors and dephasing. We numerically simulate the relationship between these noise types and the precision of the estimation. Fig. S12a shows the sum of variance in the estimated gradient as a function of different dephasing rates Γ_ϕ , while Fig. S12b depicts the effect of varying gate errors ϵ_σ on the precision. The dephasing noise is modeled using a thermal channel, and gate errors are incorporated through a Pauli noise

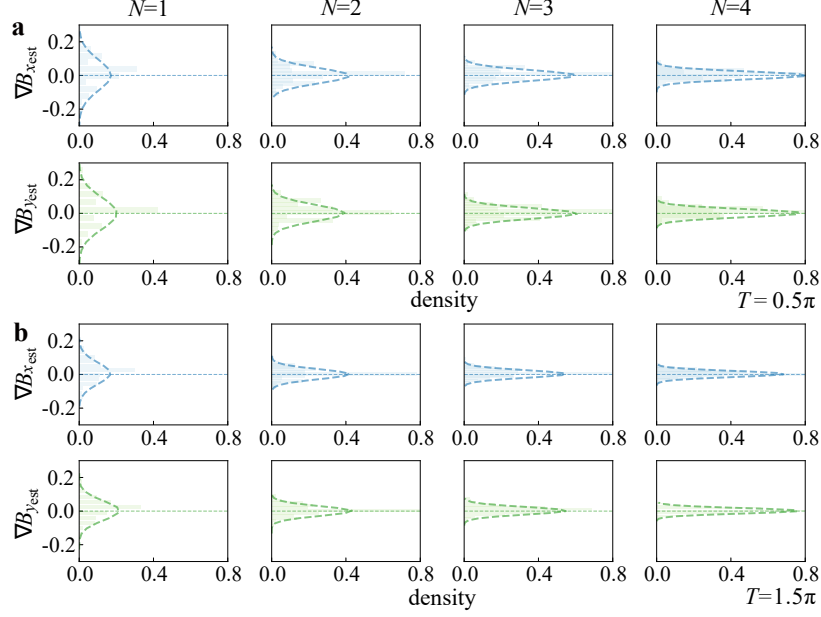


Fig. S11. **The density distribution for estimated x and y components of the vector field gradient.** Bars: MLE result histograms. Dashed curves: gaussian fitting of the histograms. Dashed lines: the ideal signal parameters. **a**, The density at $T = 0.5\pi$ for $N = 1, 2, 3, 4$. **b**, The density at $T = 1.5\pi$ for $N = 1, 2, 3, 4$.

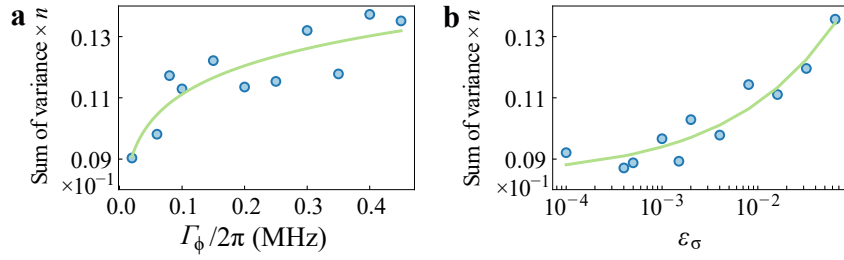


Fig. S12. **The influence of circuit error on the MLE result.** Dots: simulation data. Solid curves: fitting result. **a** The relation between simulated precision and dephasing rate. **b** The relation between simulated precision and gate error.

channel. These simulations are conducted using the Qiskit framework [14].

To mitigate the effects of noise, we apply error mitigation (EM) techniques [15] during data post-processing. For the NLE strategy, non-local entangled states are particularly sensitive to environmental noise. However, EM significantly improves performance, as demonstrated in Fig. S13.

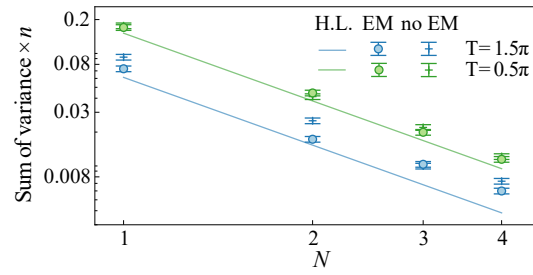


Fig. S13. The effect of error mitigation (EM) on the experimental sum of variance.

-
- [1] Yuan, H. Sequential feedback scheme outperforms the parallel scheme for hamiltonian parameter estimation. *Phys. Rev. Lett.* **117**, 160801 (2016).
- [2] Hou, Z. *et al.* Minimal tradeoff and ultimate precision limit of multiparameter quantum magnetometry under the parallel scheme. *Phys. Rev. Lett.* **125**, 020501 (2020).
- [3] Niu, J. *et al.* Low-loss interconnects for modular superconducting quantum processors. *Nat. Electron.* **6**, 235–241 (2023).
- [4] Sung, Y. *et al.* Realization of high-fidelity cz and zz-free iswap gates with a tunable coupler. *Phys. Rev. X* **11**, 021058 (2021).
- [5] Goss, N. *et al.* High-fidelity qutrit entangling gates for superconducting circuits. *Nat. Commun.* **13** (2022).
- [6] Kuroda, M., Mori, Y. & Iizuka, M. *Initial Value Selection for the Alternating Least Squares Algorithm*, 227–239 (Springer Singapore, 2020).
- [7] Hou, Z. *et al.* Zero-trade-off multiparameter quantum estimation via simultaneously saturating multiple heisenberg uncertainty relations. *Sci. Adv.* **7**, eabd2986 (2021).
- [8] Le, T. K., Nguyen, H. Q. & Ho, L. B. Variational quantum metrology for multiparameter estimation under dephasing noise. *Sci. Rep.* **13** (2023).
- [9] Yuan, H. & Fung, C.-H. F. Quantum parameter estimation with general dynamics. *npj Quantum Inf.* (2017).
- [10] Escher, B. M., de Matos Filho, R. L. & Davidovich, L. General framework for estimating the ultimate precision limit in noisy quantum-enhanced metrology. *Nat. Phys.* **7**, 406–411 (2011).
- [11] Wang, K. *et al.* Entanglement-enhanced quantum metrology in a noisy environment. *Phys. Rev. A* **97**, 042112 (2018).
- [12] Chaves, R., Brask, J. B., Markiewicz, M., Kołodyński, J. & Acín, A. Noisy metrology beyond the standard quantum limit. *Phys. Rev. Lett.* **111**, 120401 (2013).
- [13] Peng, J.-X., Zhu, B., Zhang, W. & Zhang, K. Enhanced quantum metrology with non-phase-covariant noise. *Phys. Rev. Lett.* **133**, 090801 (2024).
- [14] Javadi-Abhari, A. *et al.* Quantum computing with qiskit (2024). arXiv:2405.08810.
- [15] Conlon, L. O. *et al.* Approaching optimal entangling collective measurements on quantum computing platforms. *Nat. Phys.* **19**, 351–357 (2023).